Methods for prediction of wave kinematics

by

Pau Mercadé Ruiz

pmerca12@student.aau.dk

Master Thesis

February – June 2014

School of Engineering and Science

Aalborg University

Supervised by Thomas Lykke Andersen

Abstract

Calculation of loads caused by waves in offshore and shore structures is a recurrent practice in coastal engineering. To this purpose, accurate wave kinematics prediction is essential, especially at the free surface where velocities and accelerations are the largest. For regular waves the Stream Function Wave Theory is widely accepted and used. For irregular waves a Local Fourier approximation method exists. Such methodology is focused on exactly satisfy the free surface boundary conditions in a moving local window through a Local Fourier approximation of the velocity potential.

The Local Fourier approximation method is implemented in MatLab and tested against both stream function waves and laboratory experiments of irregular waves. Analysis of the results shows perfect agreement with predictions from Stream Function Wave Theory and with laboratory measurements.

Table of contents

1. Introduction and motivation

It is well known that waves can lead to significant loads to offshore and shore structures. To this purpose, a reliable and accurate prediction of wave kinematics, i.e. velocity and acceleration, is needed and especially at the water free surface where wave kinematics is more extreme.

Two kind of water waves are distinguished which correspond to regular and irregular waves. In this way, regular waves are characterized to maintain a permanent form, which requires the wave to be periodic and symmetric in space and time around the crest, whereas irregular waves are characterized by spatial and time randomness.

The Stream Function Wave Theory is widely accepted to best cope with regular waves and which in turn has the advantage of leading to a fast computation time, thus it is commonly used to predict kinematics for such kind of waves.

On the one hand, Computational Fluid Dynamics based methods are seen to provide accurate kinematics prediction for irregular waves, while on the other hand, they are computationally expensive requiring much more memory usage and longer computation time than other existing methods.

An alternative method to predict irregular wave kinematics is the stretching method of Wheeler which has the advantage of leading to a fast computation time but it also has the inconvenient of being based on linear wave theory. Therefore, it will lead to inaccurate kinematics prediction for nonlinear waves and especially at the free surface.

A Local Fourier approximation method was presented by Rodney J. Sobey in order to predict irregular wave kinematics which is a generalization of the Stream Function Wave Theory. Hence, it will consume less memory and perform faster than Computational Fluid Dynamics based methods and it is also expected to provide better kinematics prediction than the stretching method of Wheeler for nonlinear waves.

Therefore, the present Master's Thesis is meant to provide a Local Fourier approximation code in MatLab in order to predict accurate and reliable irregular wave kinematics at the free surface as an essential tool for further load calculations on offshore and shore structures.

1.1. Scope of the work

The present Master's Thesis is focused on the following main objectives:

- Implementation of a Stream Function Wave Theory based method, the stretching method of Wheeler and the Local Fourier approximation method in MatLab.
- Test the Local Fourier approximation method against nonlinear stream function waves and compare with Wheeler stretching kinematics prediction.

- Test the Local Fourier approximation method against laboratory experiments of irregular waves and compare with Wheeler stretching kinematics prediction.

1.2. Definitions and notation

The following wave parameters and kinematic variables and spatial and time variables are recurrently used throughout the thesis:

t	time
x	horizontal coordinate
z	vertical coordinate, where z=0 corresponds to the Mean Water Level (MWL)
h	water depth
T	wave period
L	wave length
H	wave height
$\omega_0 = 2\pi/T$	wave frequency
$k = 2\pi/L$	wave number
η	free surface elevation
$\bar{\eta} = 0$	Average free surface elevation (MWL)
ϕ	velocity potential
$u = \partial\phi/\partial x$	horizontal particle velocity
$w = \partial\phi/\partial z$	vertical particle velocity
$\boldsymbol{V} = (u, w)$	velocity vector

2. The boundary-value problem

The present study deals with methods for predicting wave kinematics. To this purpose, a mathematical approach of such problem must be firstly found and inspected in order to be finally solved.

Irregular waves were said to be characterized by spatial and time randomness. For instance, a storm event in the sea will bring about a bunch of waves travelling in different directions with different wave periods, lengths and heights and which will eventually interact and give rise to a random undulated sea surface. However, this observed irregular wave pattern might turn into a regular swell far from where they were generated.

Even though irregular and regular waves do not appear to have much in common, it will be seen that most of the problem formulation for regular waves will remain valid for irregular waves. In this regard, a general formulation in water-waves mechanics problem will be inspected and the specific considerations and assumptions for regular waves will be pointed out pertinently.

On the other hand, the problem formulation given in the following chapter is based on the assumption that water is a continuum medium (i.e. the mass is continuously distributed throughout the water). The mathematical implication of such assumption is that further problem formulation and studied principles (conservation of mass and conservation of linear momentum) will be able to be done by means of continuous functions and eventually continuously differentiable (water density, pressure field, velocity field, etc.) which is required for differential analysis (divergence theorem, Taylor series expansion, etc.), see Appendix A.1, A.2 and A.3.

2.1. Formulation in water-wave mechanics problem

In this chapter the governing hydrodynamic equations and boundary conditions that rule fluid motion in water-waves will be given. Besides, the assumptions taken into account for problem formulation will be announced and discussed.

The problem formulation in water-waves consists of a system of 2 partial differential equations, which yield from applying conservation of mass and linear momentum, and boundary conditions at the free surface (top), bottom and laterals, i.e. periodicity condition for regular waves.

Assumptions

The considered assumptions taken into account in problem formulation are incompressible fluid, irrotational flow, 2-D plane flow and inviscid flow.

Assuming incompressible fluid in water-wave mechanics problems is a regular practice since density variations in sea water are usually rather negligible.

With regard to irrotational flow assumption, it must be taken into account that vortices are generated near bottom boundary, where viscous effects play an important role (boundary layer). In this regard, it seems apparent that some vortices created within the boundary layer will be transported outside and so they will affect the flow outside the boundary layer. On the other hand, the boundary layer might grow affecting the whole flow so that irrotational flow would no longer be a suitable assumption. However, the boundary layer is observed to remain thin (i.e. thickness of the boundary layer is much smaller than water depth) and transported vortices outside the boundary layer are observed to vanish.

The velocity at the bottom boundary is seen to be a horizontal oscillation and so it will periodically change sign at the same time a new boundary layer will arise, which will cause the boundary layer to remain thin. Furthermore, the same oscillatory flow will bring about vortices constantly changing sign and so nearly all of them will be destroyed.[1]

On the other hand, the flow outside the boundary layer is inviscid and the external forces acting on it are mainly conservative (gravitational forces are dominant). Thus if irrotational flow is considered as initial condition, by Kelvin circulation theorem, the flow will remain irrotational.[1]

Overall, irrotational flow appears to be a suitable assumption which is in accordance with observations.

Furthermore, it must be said that assuming plane flow limits on the study of the so-called long-crested waves.[1]

Finally, it must be said that assuming inviscid flow is in accordance with the fact that the boundary layer is observed to remain thin, as mentioned before, and so the viscous effects will be bounded to a slim region close to the bottom whereas the rest of the flow will be inviscid.

Governing hydrodynamics equations

The first governing equation is obtained from mass conservation principle for an incompressible fluid and plane irrotational flow, which yields the so-called Laplace's equation, see Appendix A.1.

$$\frac{\partial^2 \Phi}{\partial x^2} + \frac{\partial^2 \Phi}{\partial z^2} = 0 \tag{2. 1}$$

The second governing equation is obtained from conservation of linear momentum for an inviscid flow, which yields the so-called Euler's equations of motion, and which is further developed considering incompressible fluid and plane irrotational flow yielding the so-called Unsteady Bernoulli's equation, which is an integrated form of the Euler's equations of motion, see Appendix A.2.

$$gz + \frac{p}{\rho} + \frac{1}{2}\left(\left(\frac{\partial \Phi}{\partial x}\right)^2 + \left(\frac{\partial \Phi}{\partial z}\right)^2\right) + \frac{\partial \Phi}{\partial t} = B \tag{2. 2}$$

Where the acceleration of gravity is considered as $\boldsymbol{g}=(0,0,-g)$, p is the pressure field, ρ is the water density and B is known as the Bernoulli constant which is constant in all spatial directions but it is function of time.

Boundary conditions

With regard to the bottom boundary, constant depth is assumed. As long as the bottom slope is small, constant depth is a suitable assumption which introduces simplicity to the problem formulation.

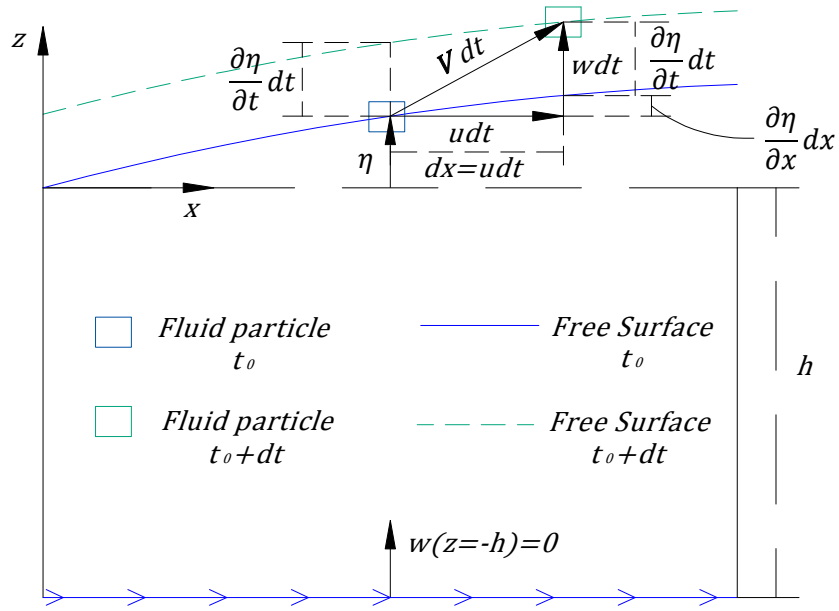

Fig. 2. 1. Sketch of the bottom boundary condition and the kinematic free surface boundary condition. It can be seen the geometrical interpretation of considering that the free surface moves together with the fluid particles on it.

No flow through the bottom boundary is imposed (Fig. 2. 1.):

$$\begin{aligned} w &= 0 \\ \frac{\partial \Phi}{\partial z} &= 0 \end{aligned} \quad at\ z = -h \tag{2. 3}$$

The following two boundary conditions are imposed at the free surface. It must be noticed that part of the complexity in solving water-wave mechanics problems stems from the fact that the free surface elevation is an unknown function and due to nonlinearity of both free surface boundary conditions.

Kinematic Free Surface Boundary Condition (KFSBC) states that the free surface must move together with the fluid particles at the free surface (Fig. 2. 1). Thereby, the kinematic condition for the free surface elevation is:

$$\begin{aligned} w &= \frac{d\eta}{dt} = \frac{\partial \eta}{\partial t} + u\frac{\partial \eta}{\partial x} \\ \frac{\partial \Phi}{\partial z} &= \frac{\partial \eta}{\partial t} + \frac{\partial \Phi}{\partial x}\frac{\partial \eta}{\partial x} \end{aligned} \quad at\ z = \eta \tag{2. 4}$$

Dynamic Free Surface Boundary Condition (DFSBC) states that at the free surface the pressure will be the atmospheric pressure. Hereby, pressure reference is decided to be the atmospheric pressure and so it is further worked with relative pressures. Therefore, Bernoulli equation at the free surface must be:

$$g\eta + \frac{1}{2}\left(\left(\frac{\partial \Phi}{\partial x}\right)^2 + \left(\frac{\partial \Phi}{\partial z}\right)^2\right) + \frac{\partial \Phi}{\partial t} = B \quad at\ z = \eta \tag{2. 5}$$

The following condition is just regarded for regular waves. Thereby, it is assumed that wave is periodic in space and time, such that:

$$\begin{matrix} \Phi(x,z,t) = \Phi(x+nL,z,t) = \Phi(x,z,t+nT) \\ \eta(x,t) = \eta(x+nL,t) = \eta(x,t+nT) \end{matrix} \quad n = 1,2,\dots \tag{2. 6}$$

Summarization of problem formulation and general comments

The boundary-value problem that must be faced is presented in the following table:

Table 2. 1. Summarization of the boundary-value problem in water-waves mechanics.

	Boundary-Value Problem for Water-Waves			Unknowns	
Field Equation		$\frac{\partial^2 \Phi}{\partial x^2} + \frac{\partial^2 \Phi}{\partial z^2} = 0$			Φ
Boundary Conditions	$i.$	$\frac{\partial \Phi}{\partial z} = 0$	$at\ z = -h$	$i.$	Φ
	$ii.$	$\frac{\partial \Phi}{\partial z} = \frac{\partial \eta}{\partial t} + \frac{\partial \Phi}{\partial x}\frac{\partial \eta}{\partial x}$	$at\ z = \eta$	$ii.$	Φ, η
	$iii.$	$g\eta + \frac{1}{2}\left(\left(\frac{\partial \Phi}{\partial x}\right)^2 + \left(\frac{\partial \Phi}{\partial z}\right)^2\right) + \frac{\partial \Phi}{\partial t} = B$	$at\ z = \eta$	$iii.$	Φ, η, B
Additional Condition for Regular Waves	$iv.$	$\Phi(x,z,t) = \Phi(x+nL,z,t) = \Phi(x,z,t+nT)$ $\eta(x,t) = \eta(x+nL,t) = \eta(x,t+nT)$	$n = 1,2,\dots$	$iv.$	L, T

Furthermore, the regarded assumptions for the water-wave mechanics problem are:

- Irrotational flow
- Inviscid flow
- 2D plane flow (Long-crested waves)
- Incompressible fluid
- Constant water depth

Therefore, Laplace's equation is the differential equation that must be solved subjected to both the nonlinear boundary conditions at the free surface (KFSBC and DFSBC) and the bottom boundary condition in order to calculate irregular wave kinematics. On the other hand, regular wave kinematics is calculated introducing also the periodicity condition.

Even though the velocity potential turns up into the Unsteady Bernoulli's equation, it can be solved separately from Laplace's equation since the pressure field is not actually appearing in the boundary conditions. Therefore, the boundary-value problem (Table 2. 1) is used for

obtaining wave kinematics whereas the pressure field can be solved from the Unsteady Bernoulli's equation, once the velocity potential is calculated.

On the other hand, due to nonlinearity of the boundary conditions at the free surface (KFSBC and DFSBC) together with the fact that the free surface elevation is an unknown of the problem, the studied boundary-value problem does not have an analytical general solution.

Hereby, there is not a straight forward way to solve such problem and several methodologies are currently available which try to find an approximated solution to the studied boundary-value problem for particular case scenarios.

In the next subchapter a method meant for regular waves and based on the Stream Function Wave Theory is presented and further implemented in MatLab.

2.2. Stream Function Wave Theory

The Stream Function Wave Theory[3] (SFWT) deals with regular waves which were said to be periodic. Thus if a frame of reference X–Z–system moving together with the wave at constant phase speed $C=\omega_0/k$ is chosen for such type of waves, the water-wave mechanics problem will become steady. In this regard, the problem formulation studied in the previous subchapter will be revisited and set up for the moving X–Z–system so as to obtain an easier-handling steady formulation.

Steady formulation

The relationship between the moving X–Z–system and the fixed x–z–system reads:

$$\begin{aligned} x &= X + Ct \\ z &= Z \end{aligned} \tag{2. 7}$$

In the same way, the relationship between the velocity components in both coordinate systems read:

$$\begin{aligned} u &= U + C \\ w &= W \end{aligned} \tag{2. 8}$$

Where U and W are the velocity components in X and Z–direction respectively.

Besides, the stream function (ψ) is used instead of the velocity potential in order to describe the flow. Thus, the relationship between the velocity components and the stream function is defined as

$$(U, W) = \left(-\frac{\partial \psi}{\partial Z}, \frac{\partial \psi}{\partial X}\right) \tag{2. 9}$$

When the velocity field is defined by means of the stream function, it can be noticed that the Laplace's equation is directly fulfilled. However, Laplace's equation is further recovered when irrotational flow is imposed (equation (A. 8)).

Therefore, the field equation turns out to be:

$$\frac{\partial^2\psi}{\partial X^2}+\frac{\partial^2\psi}{\partial Z^2}=0 \tag{2. 10}$$

On the other hand, it can be noticed that ψ=constant yields a streamline. In this regard, a differential of ψ is given as:

$$d\psi=\frac{\partial\psi}{\partial X}dX+\frac{\partial\psi}{\partial Z}dZ=WdX-UdZ \tag{2. 11}$$

Therefore, substituting equation (2. 9) into (2. 11) when moving along a line with constant ψ ($d\psi$=0), yields:

$$\frac{W}{U}=\frac{dZ}{dX} \tag{2. 12}$$

Equation (2. 12) is the equation of a streamline. It is important to see that no water can flow across a streamline since it is everywhere tangent to the velocity field.

Hereby, an observer following the wave will see the flow confined between 2 streamlines, one corresponding to the free surface and the other corresponding to the sea bottom so that water will flow neither across the free surface nor across the sea bed. Nonetheless, it is important to emphasize that such flow characterization is observed according to the X–Z–system (Fig. 2. 2).

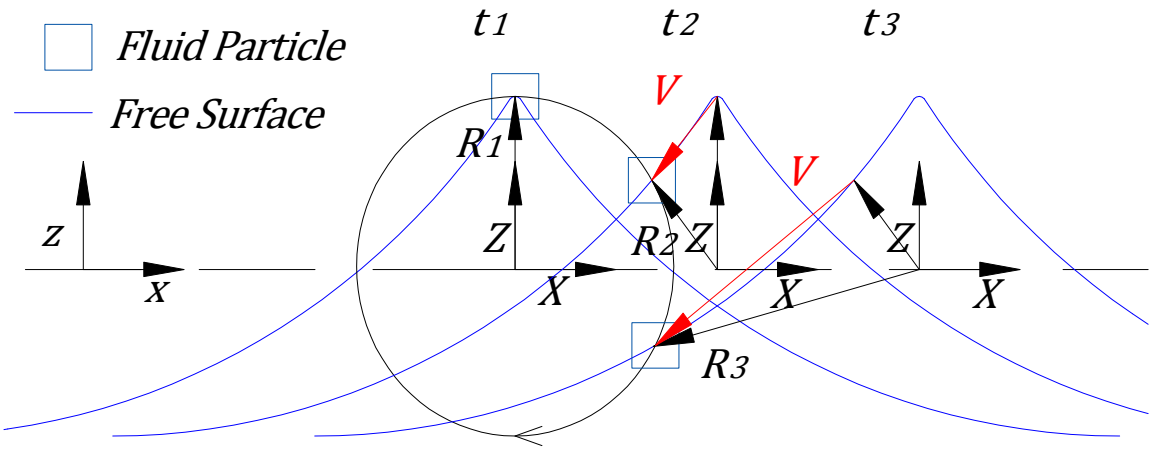

Fig. 2. 2. Simplified interpretation of the particles motion (red arrow) upon the free surface seen from a moving X–Z–coordinate system following the wave. To this purpose, the particle path seen from a fixed x–z –coordinate system has been simplified to be a closed circular orbit of diameter H.

Fig. 2. 2 sketches how a fluid particle on the free surface is observed by the X–Z–coordinate system to move away with a velocity that is tangential to the free surface. Thereby, the free surface is actually a streamline observed by the X–Z–system.

Therefore, both the bottom boundary condition (i.e. no flow across the sea bottom) and the KFSBC (i.e. no flow across the free surface) can be reformulated according to the X–Z–system as:

$$\begin{matrix} \psi = K_1 & at\ Z = -h \\ \psi = K_2 & at\ Z = \eta \end{matrix} \tag{2. 13}$$

Where K_1 and K_2 are constants.

However, K_1 and K_2 are related through the total discharge ($Q<0$) between the bottom streamline (ψ_{-h}) and the free surface streamline (ψ_η) as follows:

$$Q = -\left(\psi_\eta - \psi_{-h}\right) = K_1 - K_2 \tag{2. 14}$$

For sake of convenience $K_2=0$ is chosen and consequently $K_1=Q$. Therefore, the bottom boundary condition and the KFSBC can be rewritten as:

$$\begin{matrix} \psi = Q & at\ Z = -h \\ \psi = 0 & at\ Z = \eta \end{matrix} \tag{2. 15}$$

With regard to the DFSBC, it is reformulated as:

$$g\eta + \frac{1}{2}\left(\left(-\frac{\partial\psi}{\partial Z}\right)^2 + \left(\frac{\partial\psi}{\partial X}\right)^2\right) - B = 0 \quad at\ Z = \eta \tag{2. 16}$$

Where the partial time derivative of Φ vanishes since the regarded regular wave is steady in the X–Z–system (i.e. nothing changes throughout time for an observer following the wave).

So far, Laplace's equation, bottom boundary condition, KFSBC and DFSBC has been revisited and reformulated taking into account the stream function and the moving X–Z–system. Therefore, from now on the methodology to solve the reformulated boundary-value problem will be given.

Methodology

The method posed by the SFWT is based on an approximation of the stream function as follows:

$$\psi = Q + c_r(Z + h) + \sum_{j=1}^{N} A_j \frac{\sinh\left(jk(Z+h)\right)}{\cosh(jkh)}\cos(jkX) \tag{2. 17}$$

Where $C=c_r+C_E$ (Fig. 2. 3(a)) and C_E is the so-called uniform Eulerian current which is defined as the average horizontal velocity (over a wave-period) that a current meter would measure at level $z<\eta_{min}$.[3]

The right hand side of equation (2. 17) is a superposition of even functions ($\cos(jkX)$) which is in accordance with permanent form condition (i.e. symmetry about the crest demands even functions and periodicity is likewise guaranteed by use of $\cos(jkX)$). Indeed, this superposition might be interpreted as a truncated Fourier-series of an even function. Besides, it is noticed that the amplitude term of the Fourier-series is exponentially decaying with depth which is a feature of the SFWT.

The c_r term of equation (2. 17) introduces the constant moving away horizontal velocity along the X–direction seen by an observer moving with the X–Z–system (Fig. 2. 3(b)). In this way, the sum term will provide velocities due to the oscillatory motion whereas the c_r term will provide velocities due to the constant translational motion. Hereby, if C_E is non-zero, it should be discounted from C in order to get the proper relative constant translational motion between the fluid particles and the moving X–Z–system (Fig. 2. 3(a)). Therefore, the superposition of both oscillatory motion and relative constant translational motion will provide the fluid particle velocity seen by an observer moving with the X–Z–system.

The Q term will make the approximated stream function directly fulfil the bottom boundary condition (equation (2. 15)).

Furthermore, it can be noticed that the approximated stream function directly fulfils Laplace's equation.

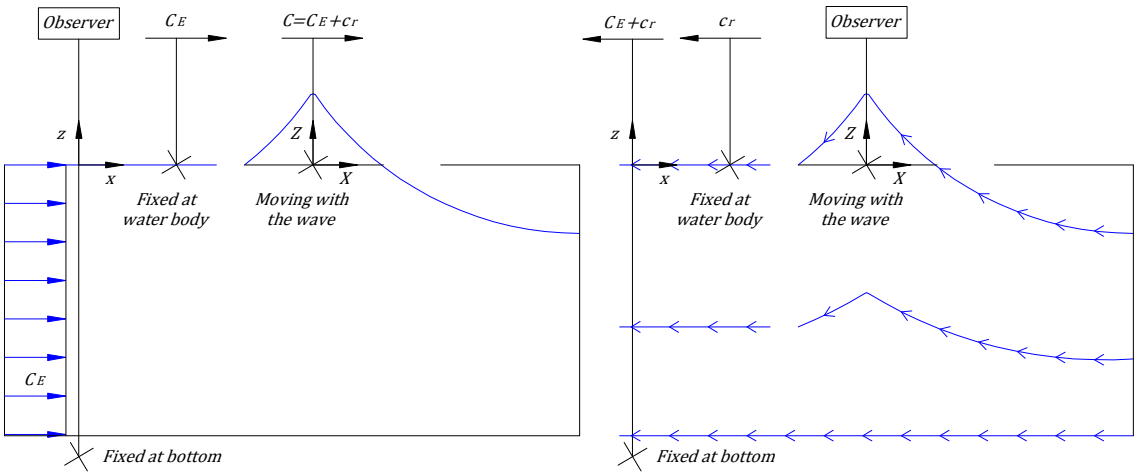

Fig. 2. 3. (a) Relationship between C_E, C and c_r seen from an observer fixed at the bottom. **(b)** Relationship between C_E, C and c_r seen from an observer travelling with the wave.

Overall, the approximated stream function given by the SFWT directly fulfils the periodicity condition, the bottom boundary condition and the Laplace's equation. Therefore, the KFSBC and the DFSBC still need to be solved.

The SFWT is based on imposing both KFSBC and DFSBC to $N+1$ points at the free surface where the corresponding η–values are unknowns of the problem. Thus, total number of equations turns out to be $2N+2$ and total number of unknowns is η_i $(N+1)$, from the evaluated points; A_j (N), c_r, k and Q, from the approximated stream function; and B, from the DFSBC; so that $2N+5$ unknowns. Therefore, there are 3 equations missing in order to have a uniquely defined system of equations.

Considering conservation of mass, the total mass of the water body must be always the same as long as there are no sinks or sources of water mass. Moreover, if the fluid is incompressible, the total volume of the water body will be always the same, as a consequence of mass conservation. If a wave-length is regarded, the volume changes experienced by the water body will be at the laterals ($X=-L/2$ and $X=L/2$) and at the MWL ($Z=0$) but at the bottom, as no water flows across it. Since the volume changes at $X=-L/2$ are balanced by the volume

changes at $X = L/2$ (due to periodicity condition), conservation of mass of an incompressible fluid corresponds to:

$$\int_{-\frac{L}{2}}^{\frac{L}{2}} \eta \, dX = 2 \int_{0}^{\frac{L}{2}} \eta \, dX = 0 \tag{2. 18}$$

Where symmetry about the crest has been considered.

Hereby, if the regarded $N+1$ η–values are set equidistantly (i.e. $\Delta X = L/N$) from crest (η_1) to trough (η_{N+1}) and considering the trapezoidal numerical integration, equation (2. 18) can be approximated as:

$$\begin{gathered} 2 \sum_{i=1}^{N} \frac{\eta_{i+1} + \eta_i}{2} \Delta X = 0 \\ \sum_{i=1}^{N} \eta_{i+1} + \eta_i = 0 \Longrightarrow \eta_{N+1} + \eta_1 + 2 \sum_{i=2}^{N} \eta_i = 0 \end{gathered} \tag{2. 19}$$

Furthermore, 2 equations can be set up by use of the definitions of both wave-height and wave-celerity.

$$H = \eta_{max} - \eta_{min} = \eta_1 - \eta_{N+1} \tag{2. 20}$$

$$C = \frac{\omega_0}{k} \tag{2. 21}$$

From equation (2. 21) an extra unknown of the problem turns up, which is C, while ω_0 is regarded as an input of the problem (i.e. known quantity). Therefore, there is still missing an equation to have a uniquely defined system of equations.

If the uniform Eulerian current is known, the relationship between C and c_r shown in Fig. 2. 3(a) can be used as required extra equation.

$$C = C_E + c_r \tag{2. 22}$$

On the other hand, if the average discharge observed by the system fixed at the bottom ($\bar{q}$) is known, the following equation can be used instead:

$$\bar{q} = Q + Ch \tag{2. 23}$$

The SFWT method is outlined in the following table:

Table 2. 2. Numerical problem posed by the SFWT which consists of a square system of nonlinear equations usually solved by use of Newton Raphson method.

In	Equations	Out
H ω_0 h g N	$\vdots$ $Q + c_r(\eta_i + h) + \sum_{j=1}^{N} A_j \frac{\sinh\left(jk(\eta_i + h)\right)}{\cosh(jkh)} \cos(jkX_i) = 0 \Big\vert_{i=1,\cdots,N+1}^{KFSBC}$ $\vdots$ $\vdots$ $g\eta_i + \frac{1}{2}\left(\left(-c_r - k\sum_{j=1}^{N} jA_j \frac{\cosh(jk(\eta_i + h))}{\cosh(jkh)} \cos(jkX_i)\right)^2 + \left(-k\sum_{j=1}^{N} jA_j \frac{\sinh(jk(\eta_i + h))}{\cosh(jkh)} \sin(jkX_i)\right)^2\right) - B = 0 \Big\vert_{i=1,\cdots,N+1}^{DFSBC}$ $\vdots$ $\eta_{N+1} + \eta_1 + 2\sum_{i=2}^{N} \eta_i = 0$ $\eta_1 - \eta_{N+1} - H = 0$ $\frac{\omega_0}{k} - C = 0$	η_1 $\vdots$ η_{N+1} A_1 $\vdots$ A_N c_r k Q B C
C_E	$C_E + c_r - C = 0$	
$\bar{q}$	$Q + Ch - \bar{q} = 0$	

Table 2.2 shows that the problem consists of a system of $2N+5+(1)$ nonlinear equations with $2N+6$ unknowns or outputs.

In order to solve the problem from Table 2.2, Newton-Raphson method is seen to be satisfactory. Therefore, since it is based on an iterative procedure, an initial estimation of the unknown parameters is required.

In this way, Airy wave theory is seen to provide a satisfactory initial estimate of k through the dispersion relationship:[1]

$$gk\tanh(kh) - \omega_0 = 0 \tag{2. 24}$$

From the initial estimate of k it follows:

$$c_r = \frac{\omega_0}{k} \tag{2. 25}$$

$$\begin{cases} C = c_r + C_E & if\ C_E\ is\ known \\ C = c_r & if\ C_E\ is\ unknown \end{cases} \tag{2. 26}$$

Where it should be noticed that the dispersion relationship corresponds to 1rst order theory (Airy wave theory) so that it will provide k taking into account ω_0 with respect to the water body and so c_r. This is so since the uniform Eulerian current corresponds to a higher order term which is disregarded in Airy wave theory.

Initial estimates of η–values are also calculated by means of Airy free surface elevation solution:[1]

$$\eta_i = \frac{H}{2}\cos(kX_i) \quad i = 1, \cdots, N+1 \tag{2. 27}$$

Besides, A_1 can be initially guessed taking into account the Airy vertical velocity[1] and set it equal to the vertical velocity calculated from the approximated stream function for N=1. The rest of A_j coefficients can be set to zero as initial estimates.

$$\begin{aligned} A_1 &= -\frac{\omega_0 H}{2k\tanh(kh)} \\ A_j &= 0 \quad j = 2, \cdots, N \end{aligned} \tag{2. 28}$$

The average discharge through a vertical section reads:

$$Q = \int_{-h}^{\bar{\eta}} \bar{U}\, dZ \tag{2. 29}$$

Where $\bar{U}$ is the average horizontal velocity seen by an observer in the X–Z–system.

Since $\bar{U} = -c_r$, Q initial estimate is decided as:

$$Q = -c_r h \tag{2. 30}$$

On the other hand, if the average relative pressure at the bottom ($\overline{p_b}$) is approximated as:[4]

$$\overline{p_b} = \rho g(h + \bar{\eta}) \tag{2. 31}$$

The average Bernoulli constant ($\bar{B}$) will be:

$$\bar{B} = g(-h) + \frac{\overline{p_b}}{\rho} + \frac{1}{2}\overline{U_b^2} \Rightarrow \bar{B} = g\bar{\eta} + \frac{1}{2}\overline{U_b^2} \tag{2. 32}$$

Where $\overline{U_b^2}$ is the average squared horizontal velocity at the bottom seen by an observer in the X–Z–system.

If the averaged squared horizontal velocity is approximated as $c_r{}^2$ the initial estimate of B can be set to:

$$B = \bar{B} = \frac{1}{2}c_r^2 \tag{2. 33}$$

Finally, it must be said that presented initial estimates are not always sufficiently good in order to achieve convergence to the solution. Since initial estimates are mainly based on Airy wave theory, problems in convergence will be found when dealing with markedly nonlinear waves. In order to overcome this problem, the SFWT can be performed in several steps with successive wave-height increments (ΔH) where the initial guesses in the iteration are updated at every step by use of the solution obtained in the previous step.

2.3. The stretching method of Wheeler

In order to calculate irregular wave kinematics, Wheeler presented a method the so-called stretching method of Wheeler which is meant to calculate kinematics from a measured free surface time history (η_i with i=1,2,…,I) which is further transformed into a Fourier-series so that the kinematics of each identified linear component ($\dot{\eta}_f$ with f=0,1,…,$F/2$) is calculated through Airy kinematics solution[1] along with an empirical transformation on each measured free surface elevation (η_i). In this subchapter the stretching method of Wheeler is outlined and further implemented in MatLab.

Firstly a zero-down crossing analysis is performed so that η_1 corresponds to the measured free surface elevation at the first zero-down crossing time (t_1) and η_I corresponds to the measured free surface elevation at the last zero-down crossing time (t_I), or alternatively the analysis can be done with zero-up crossings.

Secondly a Fast Fourier Transformation is performed from the η_i–values so as to decompose the irregular free surface elevation time record into a finite number (i.e. $F = I-1$) of linear waves ($\dot{\eta}_f$) of amplitude A_f and B_f such that:

$$\begin{aligned} \dot{\eta}_f &= A_f \cos(f\omega_0 t) + B_f \sin(f\omega_0 t) \quad f = 0,1,\dots,F/2 \\ \eta_i &= \sum_0^{F/2} \dot{\eta}_f(t_i) \qquad\qquad i = 1,2,\dots,I \end{aligned} \tag{2. 34}$$

Where $\omega_0 = 2\pi \,/\, (t_I - t_1)$.

Consequently the corresponding variance spectrum, in which the spectral density is defined as: $S_\eta = 1/2\ (A^2{}_f + B^2{}_f) \,/\, (1 \,/\, (t_I - t_1))$[5] with f=0,1,…,$F/2$; might be filtered before kinematics is calculated, see chapter 5.

Finally, kinematics is calculated through Airy kinematics solution for each $\dot{\eta}_f$ along with an empirical transformation which stretches or shrinks the velocity profile along depth from the MWL to the local free surface elevation (η_i).

Therefore, the horizontal velocity is predicted as:

$$u_i = C_E + \sum_0^{F/2} f\omega_0 \frac{\cosh(\alpha_i k_f h)}{\sinh(k_f h)} \dot{\eta}_f(t_i) \quad i = 1,2,\dots,I \tag{2. 35}$$

Where $\alpha_i = (h + z) \,/\, (h + \eta_i)$ and k_f is calculated from the linear dispersion relationship (2. 24) and by use of $f\omega_0$ so that each linear component ($\dot{\eta}_f$) satisfies the linear dispersion relationship.

The vertical velocity and the horizontal acceleration predictions are obtained from Sobey[2] since Wheeler does not give estimators for them.

$$w_i = -\sum_0^{F/2} f\omega_0 \frac{\sinh(\alpha_i k_f h)}{\sinh(k_f h)} \hat{\eta}_f(t_i) \quad i = 1,2,\dots,I \tag{2. 36}$$

and:

$$\left(\frac{du}{dt}\right)_i \approx \left(\frac{\partial u}{\partial t}\right)_i = -\sum_0^{F/2} (f\omega_0)^2 \frac{\cosh(\alpha_i k_f h)}{\sinh(k_f h)} \hat{\eta}_f(t_i) \quad i = 1,2,\dots,I \tag{2. 37}$$

Where the $\hat{\eta}_f(t_i)$ sum to $\hat{\eta}(t_i)$ is the Hilbert transform of η so that:

$$\begin{aligned} \hat{\eta}_f &= A_f \sin(f\omega_0 t) - B_f \cos(f\omega_0 t) \quad f = 0,1,\dots,F/2 \\ \hat{\eta}(t_i) &= \sum_0^{F/2} \hat{\eta}_f(t_i) \qquad\qquad i = 1,2,\dots,I \end{aligned} \tag{2. 38}$$

3. Local Fourier approximation method for irregular waves

In order to calculate irregular wave kinematics, Sobey[2] presented a Local Fourier (LF) approximation method which is meant to calculate kinematics from a measured free surface time history by means of a local approximation of the velocity potential as a truncated Fourier-series (equation (3. 1)). In this chapter LF approximation method is presented and further implemented in MatLab.

$$\phi = C_E x + \sum_{j=1}^{J} A_j \frac{\cosh\big(jk(z+h)\big)}{\cosh(jkh)} \sin\big(j(kx - \omega_0 t)\big) \tag{3. 1}$$

The main difference between the SFWT and the LF approximation method is that the first is exclusive for regular waves while the second is also meant for irregular waves. In this regard, it was seen that the main difference in problem formulation (Table 2. 1) was the assumption of periodicity condition for regular waves whereas Laplace's equation, bottom boundary condition, KFSBC and DFSBC had to be satisfied for both regular and irregular waves.

In this way, it is noticed that both the SFWT and the LF approximation method are based on an approximation of the stream function (global) and the velocity potential (local) respectively as a truncated Fourier-series (equations (2. 17) and (3. 1)) so that the periodicity condition is implicitly taken into account. Nonetheless, the inappropriate periodicity condition in the LF approximation method is overcome by use of a local approximation of the velocity potential so that the periodic wave parameters, ω_0 and k, will be locally defined.

Furthermore, it can be seen that the approximation of the velocity potential in the LF approximation method directly satisfies Laplace's equation and the bottom boundary condition as it was also seen to satisfy the approximation of the stream function in the SFWT.

Unlike the SFWT, the LF approximation method does not seek to predict the free surface elevation and so kinematics are estimated from a measured free surface time history. Thus, there is a lack of spatial free surface information which is necessary so as to calculate the spatial gradient term in the KFSBC. In this regard, the LF approximation method assumes that the free surface moves in the x–direction with local constant phase speed $C{=}\omega_0/k$ as it was seen to behave for steady regular waves (globally). Thus, the free surface is assumed to evolve locally as:

$$\frac{\partial \eta}{\partial t} + C\frac{\partial \eta}{\partial x} = 0 \tag{3. 2}$$

Therefore, spatial gradients ($\partial\eta/\partial x$) in the KFSBC can be approximated from the temporal gradients ($\partial\eta/\partial t$) by use of equation (3. 2).

Equation (3. 2) expresses that the free surface is not moving up and down throughout time but with horizontal phase speed C (Fig. 3. 1) though it must be said that is a local assumption and so C will be locally defined.

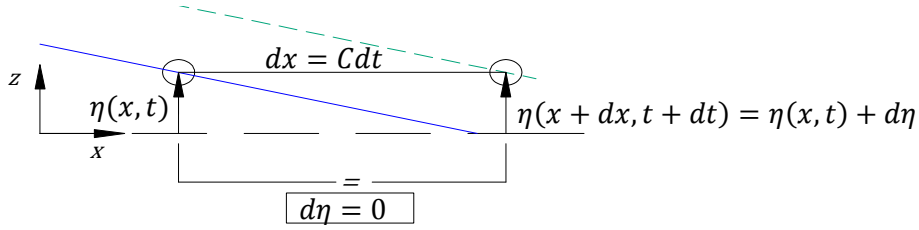

Fig. 3. 1. Geometrical interpretation of the local steady assumption. It can be seen the relationship between the spatial gradients and temporal gradients of the free surface elevation when the wave moves with constant horizontal phase speed C.

Even though the local steady assumption is not appropriate for irregular waves, it will be seen that LF approximation method prevents its overuse so as not to compromise the local solution.

The LF approximation method is based on a moving window of duration τ which is set up at every instant of time where output is decided (i.e. where kinematics is decided to be calculated which is defined by the output resolution). In order to capture the local wave behaviour, the moving window is centred at each output time-point. Besides, it must be said that locality is accomplished as long as τ is decided significantly smaller than the local zero-down or up crossing period (T_z), which is defined as the time comprised between two consecutive zero-down or up crossings (Fig. 3. 2). In this regard, a window of duration τ=0.1 T_z is typically used[3].

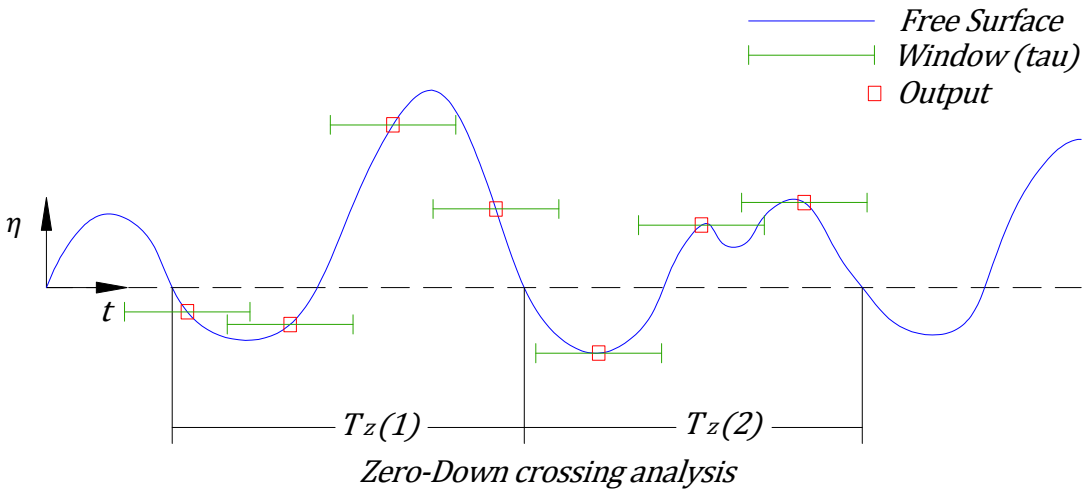

Fig. 3. 2. Sketch of the different settlements of the moving window according to the predefined output. The moving window is centred at each output node and moves from one another until the whole irregular wave profile is covered.

In the following subchapters the local formulation within the moving window as well as the local methodology followed to obtain the local solution within the moving window will be given.

3.1. Local formulation

The representation of the velocity potential at each window is based on the LF approximation given in equation (3. 1). Hence, as it was previously said, equation (3. 1) directly satisfies both Laplace's equation and the bottom boundary condition throughout the whole water domain.

Thus, the local formulation is based on imposing both the KFSBC and the DFSBC within each window.

In this way, the free surface elevation within each window is known at a discrete number of time instants (nodes) from the measured free surface time history. Therefore, the KFSBC (f^k=0) and the DFSBC (f^d=0) at each node (i=1,2,…,I) within the window reads:

$$f_i^k = w_i - \left(\frac{\partial \eta}{\partial t}\right)_i - u_i \left(\frac{\partial \eta}{\partial x}\right)_i = 0 \quad at\ z = \eta_i \tag{3. 3}$$

$$f_i^D = g\eta_i + \frac{1}{2}\left(u_i^2 + w_i^2\right) + \left(\frac{\partial \phi}{\partial t}\right)_i - B = 0 \quad at\ z = \eta_i \tag{3. 4}$$

Where the velocity components at z=η are expressed by means of the approximated velocity potential evaluated at z=η at each node as follows:

$$u_i = \frac{\partial \phi}{\partial x}(x, \eta_i, t_i) = C_E + \sum_{j=1}^{J} jkA_j \frac{\cosh\left(jk(\eta_i + h)\right)}{\cosh(jkh)} \cos\left(j(kx - \omega_0 t_i)\right) \tag{3. 5}$$

$$w_i = \frac{\partial \phi}{\partial z}(x, \eta_i, t_i) = \sum_{j=1}^{J} jkA_j \frac{\sinh\left(jk(\eta_i + h)\right)}{\cosh(jkh)} \sin\left(j(kx - \omega_0 t_i)\right) \tag{3. 6}$$

Besides:

$$\left(\frac{\partial \phi}{\partial t}\right)_i = \frac{\partial \phi}{\partial t}(x, \eta_i, t_i) = \sum_{j=1}^{J} -j\omega_0 A_j \frac{\cosh\left(jk(\eta_i + h)\right)}{\cosh(jkh)} \cos\left(j(kx - \omega_0 t_i)\right) \tag{3. 7}$$

With regard to the Bernoulli constant, it is approximated through the average Bernoulli constant ($\bar{B}$) as follows:

$$\bar{B} = g\bar{\eta} + \frac{1}{2}\overline{u_b^2} = \frac{1}{2}\overline{u_b^2} \tag{3. 8}$$

Where $\overline{u_b^2}$ is the average squared horizontal velocity at the bottom:

$$\begin{aligned} \overline{u_b^2} &= \frac{1}{T}\int_0^T \left(C_E + \sum_{j=1}^{J} jkA_j \frac{\cosh\left(jk(-h + h)\right)}{\cosh(jkh)} \cos\left(j(kx - \omega_0 t)\right) \right)^2 dt \\ &= \frac{1}{T}\int_0^T C_E^2\, dt + \frac{1}{T}\int_0^T 2\, C_E \sum_{j=1}^{J} \frac{jkA_j}{\cosh(jkh)} \cos\left(j(kx - \omega_0 t)\right) dt \\ &\quad + \frac{1}{T}\int_0^T \left(\sum_{j=1}^{J} \frac{jkA_j}{\cosh(jkh)} \cos\left(j(kx - \omega_0 t)\right) \right)^2 dt \end{aligned} \tag{3. 9}$$

It can be seen that $\overline{u_b^2}$ consists of a superposition of 3 average integrals. The first average integral directly leads to C_E^2 since it is a constant parameter. The second average integral vanishes since cosine functions are averaged. On the other hand, taking into account that the system of trigonometric functions $\left(\cos(\omega_0 t), \cos(2\omega_0 t), \ldots, \cos(N\omega_0 t)\right)$ is orthogonal on the interval $t\epsilon[0, T]$:

$$\int_0^T \cos(m\omega_0 t)\cos(n\omega_0 t)\, dt = 0 \quad \forall\, m \neq n \tag{3. 10}$$

And taking into account that the average of a squared cosine function is $1/2$, the third average integral from equation (3. 9) leads to: $1/2\sum_{j=1}^{J}\left(jkA_j/\cosh(jkh)\right)^2$.

Therefore, $\overline{u_b^2}$ can be rewritten as:

$$\overline{u_b^2} = C_E^2 + \frac{1}{2}\sum_{j=1}^{J}\left(\frac{jkA_j}{\cosh(jkh)}\right)^2 \tag{3. 11}$$

Consequently, substituting equation (3. 11) into (3. 8), the Bernoulli constant can be approximated through:

$$B = \bar{B} = \frac{1}{2}C_E^2 + \frac{1}{4}\sum_{j=1}^{J}\left(\frac{jkA_j}{\cosh(jkh)}\right)^2 \tag{3. 12}$$

It must be said that t_i in the local formulation is used as local time, which means that in the centre of the window the local time is set to zero and thus $-\tau/2 \leq t_i \leq \tau/2$.

With regard to η_i and $(\partial\eta/\partial t)_i$, they are decided to be obtained from the measured free surface time history by means of cubic spline interpolation (C2, 2 times continuously differentiable). In this way, the number of nodes within the window will not be restricted and so the desired number of nodes (i.e. window resolution) will be able to be set up freely. On the other hand, as it was previously said, $(\partial\eta/\partial x)_i$ in the KFSBC is decided to be estimated from $(\partial\eta/\partial t)_i$ by equation (3. 2).

Overall, it has been seen that local formulation consists of both the KFSBC and the DFSBC which can be imposed at each node (i=1,2,…,I) within each window.

3.2. Local methodology

The problem shown in Table 3. 1 consists of $2I$ equations and J+3 unknowns, where kx corresponds to the spatial phase that need to be determined due to the lack of spatial free surface information.

Table 3. 1. Numerical problem posed by the LF approximation method which consists of a system of nonlinear equations which will be solved as a nonlinear least squares problem.

Equations	Unknowns
$\vdots$	
$f_i^k = w_i - \left(\frac{\partial \eta}{\partial t}\right)_i - u_i \left(\frac{\partial \eta}{\partial x}\right)_i = 0 \Big\vert \begin{matrix} KFSBC \\ i = 1, \cdots, I \end{matrix}$	A_1
$\vdots$	$\vdots$
	A_J
$\vdots$	ω_0
$f_i^D = g\eta_i + \frac{1}{2}(u_i^2 + w_i^2) + \left(\frac{\partial \phi}{\partial t}\right)_i - B = 0 \Big\vert \begin{matrix} DFSBC \\ i = 1, \cdots, I \end{matrix}$	k
	kx
$\vdots$	

If M equations are selected over the available $2I$ equations, the local solution will be uniquely defined for $M{=}J{+}3$ and overspecified for $M{>}J{+}3$. In this regard, it must be said that eventually some overspecification is needed in order to converge to the solution, e.g. due to error bands in the measured free surface elevation (Fig. 3. 3).

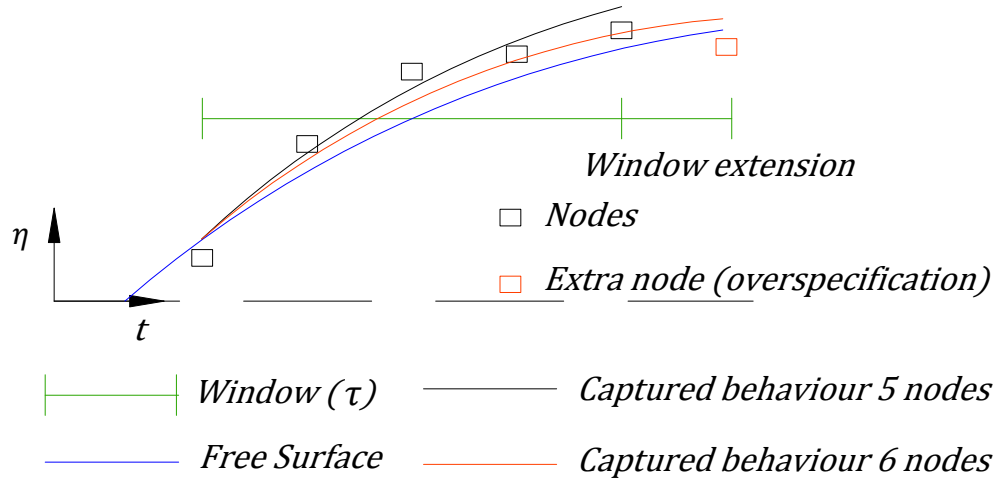

Fig. 3. 3. Sketch of error bands in the measured free surface elevation. It is shown the eventual need of incorporation of extra nodes within the window in order to reach convergence on the local solution. In other words, overspecification is sometimes advantageous since local solution is found to best fit the free surface boundary conditions.

Fig. 3. 3 illustrates that error bands might mislead the real free surface behaviour which can be overcome by the insertion of extra nodes (i.e. overspecification) until a better approximation to the free surface behaviour is achieved. The $J{+}3$ unknowns will be found to best fit both the KFSBC and the DFSBC at the I nodes (i.e. nonlinear least squares problem) and so overspecification might help to achieve convergence to the solution. On the other hand, it can be anticipated that overspecification will be implemented by an extension of the window where solely the DFSBC will be imposed so as to avoid the unnecessary usage of the local steady assumption.

In the following subchapters the implemented numerical methods to solve the problem posed in Table 3. 1 (Problem-Solving) as well as the description of how the nodes are set up within the window (window configuration) will be given and discussed.

Window configuration

The strategy adopted at each window consists on starting with $M=J+3$ and further increased until convergence is achieved or until M_{max} is reached.

$$M = J + 3, J + 4, \dots, M_{max} \tag{3. 13}$$

Moreover, as it was previously said, the successive $M>J+3$ are implemented by a window extension and imposing solely the DFSBC ($f^d=0$) to the extra nodes. In this regard, the successive window extensions are set symmetrically with respect to the centre of the window, i.e. every extension towards the positive local time direction is preceded by an extension towards the negative local time direction (Fig. 3. 4).

Starting with $M=J+3$ the required number of nodes which the window must consist of in order to have a uniquely defined system of equations is:

$$I = \text{ceil}\left(\frac{J+3}{2}\right) \tag{3. 14}$$

Where $a=\text{ceil}\,(x)$ is a function which rounds up x to the next higher integer.

With regard to the I nodes, they are set up equidistantly from local time $t_1=-\tau/2$ until $t_I=\tau/2$ giving the local time increment $\Delta t=\tau/\,(I-1)$. The KFSBC ($f^k=0$) is imposed at every node and the DFSBC ($f^d=0$) is imposed at $I\,(-1)$ nodes, i.e. it is imposed until $J+3$ equations are reached. The node where f^d might not be used (-1) for $M=J+3$ is decided to be the central node or alternatively the node at the right side from the centre. Therefore, it should be noticed that if f^d is not used at such node for $M=J+3$ it will be used afterwards when $M=J+4$ and so with no need of extending the window.

Moreover, extra nodes (I_e) for overspecification ($M>J+3$) will be set up successively as: $(-\tau/2-\Delta t, \tau/2+\Delta t, -\tau/2-2\Delta t, \tau/2+2\Delta t, \dots)$; and solely f^d will be imposed to them (Fig. 3. 4).

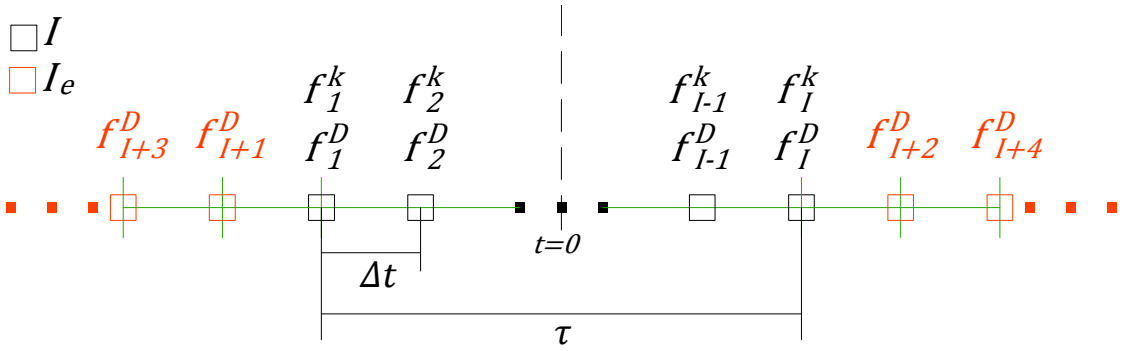

Fig. 3. 4. Sketch of how the nodes are configured within the window. It can also be seen that window extension for overspecification does not impose the kinematic free surface boundary condition at the incorporated nodes (orange).

Problem-Solving

Nonlinear least squares algorithms have been decided in order to solve the system of nonlinear equations presented in Table 3. 1 within each window 3 in total in which 2, the Levenberg-Marquardt method[6][7] and a hybrid method[7] combination of Levenberg-Marquardt and Quasi-Newton methods, were implemented in MatLab and 1, the Trust-Region-Reflective method, was directly taken from the Optimization Toolbox of MatLab used in the function "lsqnonlin". It must be said that nonlinear least squares algorithms appears to be a suitable choice since they can deal with both uniquely defined and overspecified system of equations. On the other hand, and extra algorithm, the Powell's Dog Leg method[7], was implemented in MatLab which is specially meant to find zeros of a system of N nonlinear equations with N unknowns.

Levenberg-Marquardt method (Damped method) is presented in Sobey[2] for solving the problem when it is overspecified and so it was the first one decided to be implemented. Moreover, the hybrid method was regarded in order to improve convergence to the solution though no significant advantage was observed even in those cases where Levenberg-Marquard method was underperforming. Trust-Region-Reflective method (Trust Region method) was directly used from the Optimization Toolbox of MatLab which enables the imposition of bound-constraints on the solution and which provides a different approach to the problem-solving as it is a Trust Region method. Powell's Dog Leg method (Trust Region method) was used when $M{=}J{+}3$, but it was observed that in those cases where $M{=}J{+}3$ was enough to achieve convergence the Levenberg-Marquardt method and the Trust-Region-Reflective method also made it and so there was no point to shift from one another method as M was being increased.

Every stated method requires the calculation of the Jacobian matrix (JJ). In this regard, JJ has been decided to be calculated analytically in order to reduce computation time as well as to avoid convergence to spurious solutions due to errors in the numerical approximation to the derivatives.

Since the regarded methods are based on an iterative procedure, an initial estimation of the unknown wave-parameters is required. Initial estimates are such a big deal in least squares problems since they strongly affect to the final converged solution. In this way, Sobey[2] presented a strategy for the selection of the initial estimates based on the Airy approximations to both the KFSBC and the DFSBC (equation (3. 15)) imposed at the centre of the window ignoring the solution obtained in the previous window which intends to reduce the chances to converge to spurious solutions and their further spreading.

$$\begin{aligned} w - \frac{\partial \eta}{\partial t} &= 0 \quad at\ z = 0 \\ g\eta + \frac{\partial \phi}{\partial t} &= 0 \quad at\ z = 0 \end{aligned} \tag{3. 15}$$

Therefore, substituting the approximated velocity potential with $J{=}1$ and $t{=}0$ (i.e. window centre) and $z{=}0$ into equation (3. 15) yields:

$$\begin{gathered} kA_1 \tanh(kh)\sin(kx) - \left(\frac{\partial \eta}{\partial t}\right)_C = 0 \\ g\eta_C - \omega_0 A_1 \cos(kx) = 0 \end{gathered} \tag{3. 16}$$

Where η_C and $\left(\frac{\partial \eta}{\partial t}\right)_C$ are the free surface elevation and the temporal gradient of the free surface elevation at the window centre respectively.

Therefore, solving for A_1 and kx yields:

$$\begin{gathered} A_1 = \sqrt{\left(\frac{(\partial\eta/\partial t)_C}{k\tanh(kh)}\right)^2 + \left(\frac{g\eta_C}{\omega_0}\right)^2} \\ kx = \operatorname{atan2}\left(\frac{(\partial\eta/\partial t)_C}{k\tanh(kh)}, \frac{g\eta_C}{\omega_0}\right) \end{gathered} \tag{3. 17}$$

Where θ=atan2(y,x) returns the angle θ between the positive x–axis of a plane and the vector defined from the origin to the point of coordinates (x,y) within the interval $(-\pi, \pi]$.

The rest of Fourier coefficients A_j initial estimates are assumed to be a monotonically decreasing sequence as follows:

$$A_j = \frac{A_1}{10^{j-1}} \quad for\ j = 1, \dots, J \tag{3. 18}$$

Furthermore, ω_0 is initially estimated from the local zero-down-up crossing period (T_z) as:

$$\omega_0 = \frac{2\pi}{T_z} \tag{3. 19}$$

Consequently, k is initially estimated from ω_0 through the Airy dispersion relationship (equation (2. 24))

So far, both JJ and the initial estimates have been considered so as to prevent spurious solutions. However, it is seen that followed strategy is not always successful.

In this regard, spurious solutions can be identified by negative values of ω_0, k or A_j as well as sequences of Fourier coefficients which are not monotonically decreasing, i.e. they do not follow as $A_1 > \dots > A_J$. Therefore, it is possible to define a set of inequality constraints (bound-constraints) which the solution must not violate so as to be accepted.

$$\begin{gathered} lb < q < ub \\ \begin{pmatrix} 0 \\ 0 \\ 0 \\ \vdots \\ 0 \\ 0 \\ 0 \\ -\infty \end{pmatrix} < \begin{pmatrix} A_1 \\ A_2 \\ A_3 \\ \vdots \\ A_J \\ \omega_0 \\ k \\ kx \end{pmatrix} < \begin{pmatrix} \infty \\ A_1 \\ A_2 \\ \vdots \\ A_{J-1} \\ \infty \\ \infty \\ \infty \end{pmatrix} \end{gathered} \tag{3. 20}$$

On the one hand, the Trust-Region-Reflective method from Matlab Optimization Toolbox can deal with bound-constraints in the form of upper bounds (ub) and lower bounds (lb) on the solution while on the other the Levenberg-Marquardt method is meant for unconstrained

problems. Nonetheless, the Levenberg-Marquardt method can be used for constrained nonlinear least squares with simple constraints, such as ub and lb, when it is combined with an active-set method[8][9].

The basis of the resulting combined methodology consists on splitting the variables of the problem into an active set, which consists of all the variables that violate constraints, and an inactive set, which consists of all the variables that do not violate any constraint. In this way, a reduced problem taking into account the inactive set can be solved as an unconstrained problem so that by means of the Levenberg-Marquardt method. It must be noticed that the active set and the inactive set will change at each iteration.

The modifications in the Levenberg-Marquard method to handle bound-constraints within the iteration are outlined in boldface (red) as follows

Levenberg – Marquardt iteration outline

$A := JJ(q)^T JJ(q)$

$g := JJ(q)^T f(q)$

while (not found) and $l < l_{max}$

$l := l + 1$

update $\Rightarrow ub = (\infty, q(1{:}J-1), \infty, \infty, \infty)$

solve $\Rightarrow (A + \lambda\, Id) h_{LM} = -g$

$q_{new} := q + h_{LM}$

$\boldsymbol{q_p := \max(\min(q_{new}, ub), lb)}$

$\boldsymbol{h_{LM} := q_p - q}$

if h_{LM} acceptable

$\boldsymbol{q := q_p}$

update $\Rightarrow A$ and g

$$\boldsymbol{g_p = \begin{pmatrix} \vdots \\ g_p^r \\ \vdots \end{pmatrix} \Rightarrow g_p^r := \begin{cases} g^r & \text{if } lb^r < q_p^r < ub^r \\ g^r & \text{if } q_p^r = ub^r \text{ and } g^r > 0 \\ g^r & \text{if } q_p^r = lb^r \text{ and } g^r < 0 \\ 0 & \text{otherwise} \end{cases}}$$

$$\boldsymbol{D_G = \begin{pmatrix} \ddots & & \text{Zeros} \\ & D_G^{rr} & \\ \text{Zeros} & & \ddots \end{pmatrix} \Rightarrow D_G^{rr} := \begin{cases} 1 & \text{if } lb^r < q_p^r < ub^r \\ 0 & \text{otherwise} \end{cases}}$$

$\boldsymbol{D_E = Id - D_G}$

$\boldsymbol{A := D_G A D_G + D_E}$

$\boldsymbol{g := g_p}$

$\lambda \downarrow$

found?

else

$\lambda \uparrow$

(3. 21)

Where Id, is the identity matrix, λ is the Levenberg-Marquardt damping parameter which $\lambda \geq 0$, the superscript r indicates the matrix or vector component in which $r=1,\ldots, J+3$, q is the column vector containing the wave parameters $q=(A_1,\ldots, A_J, \omega_0, k, kx)^T$ and $f(q)$ is the column vector containing f^k and f^D at every evaluated node, whose length is M.

The function a=max (x, y), where x and y are vectors of same length, returns a vector a whose components are the largest between the components of x and y. The function a=min (x, y) is analogous but returning the smallest components.

Therefore, when the parameters violate either ub or lb (active set) they are directly set to the corresponding ub^r or lb^r while the rest of wave parameters remain unchanged (inactive set) leading to the projected wave parameters vector q_p. Consecutively, if the produced step h_{LM} is acceptable, the gradient g is projected g_p according to the conditions in (3. 21) and which are illustrated in Fig. 3. 5. Hence, the approximated Hessian matrix (A) is reduced so that solely the inactive set of parameters will follow the Levenberg-Marquardt step (strictly speaking) in the next iteration but also enabling the parameters from the active set change in the direction of the $-g_p$ in the next iteration.

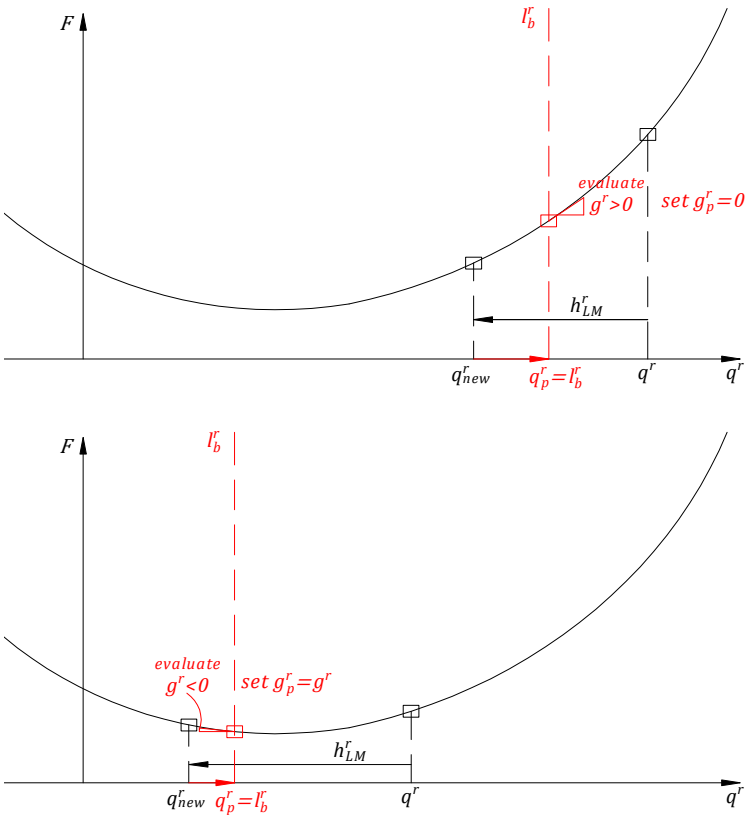

Fig. 3. 5. Simplified geometrical interpretation of the calculation of the projected gradient for the case of a lower bound lb^r on the variable q^r.

Where F= 1/2 f (q) ^{T} f (q) is the function to be minimized.

It must be said that the Trust-Region-Reflective method from MatLab can handle bound-constraints as an available option though ub cannot be updated at every step in the iteration in order to make the Fourier coefficients fulfil the sequence A_1>…> A_J. Therefore, spurious solutions are eventually found when using such method. On the other hand, the methodology presented in (3. 21) enables an update of ub at every step in the iteration from the current estimate of the solution q.

3.3. Summarization and general comments

In the next figure the LF approximation method is summarized.

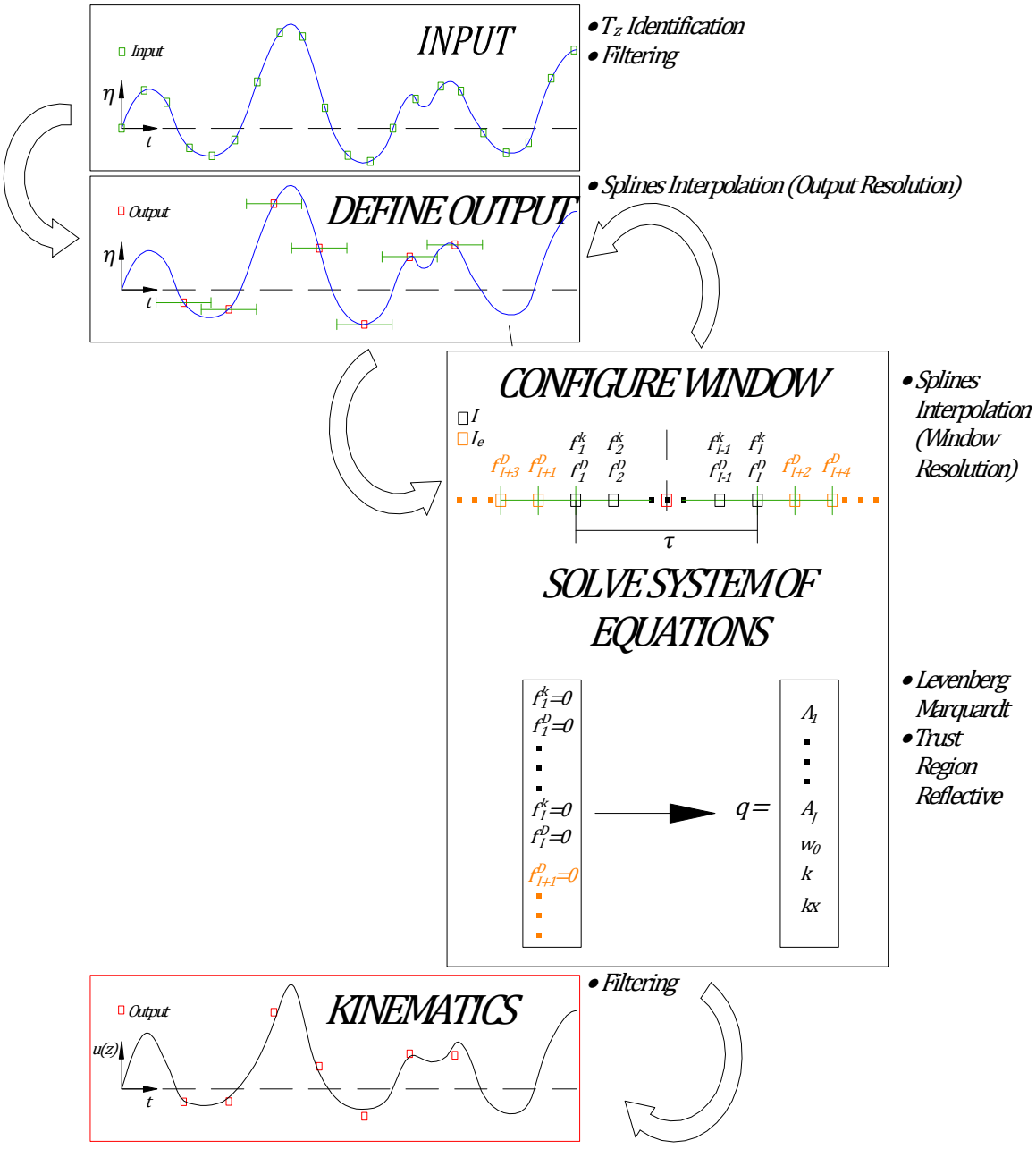

Fig. 3. 6. Summarization of the procedure followed for the LF approximation method.

Firstly a zero-up-down crossing analysis is performed from the free surface record and so the set of T_z is identified, which will be further required to define τ as well as to calculate the initial estimate of ω_0 at each window. Secondly, the output is defined and so the corresponding η and $\partial\eta/\partial t$ at each output node are obtained. Thirdly, iteration is started while the local window is moving from one output node to another. Therefore, at every window settlement the window is configured according to the decided J and M_{max} and the corresponding τ so that

the system of equations can be set up and solved to obtain q. The iteration stops when the local window reaches the last output node so that q has been obtained at every window. Finally, the wave kinematics can be calculated from q obtained at each window.

It is seen that cubic splines interpolation is a useful tool to calculate temporal gradients ($\partial\eta/\partial t$) but also in order to obtain the desired resolution on the output (output resolution) and within the moving window (window resolution). On the one hand, the output resolution is user defined so that wave kinematics can be calculated at every desired instant of time while on the other the window resolution (I and I_e nodes) will depend on the choice of J and M_{max}.

Besides, both the input (i.e. measured free surface time history) and the output (i.e. calculated wave kinematics) are subjected to a moving average filter, which its half width corresponds to: $s{=}L_f\ \mathrm{round}\ ((\tau/\ \Delta t{-}1)/2)$; where the function $a{=}\mathrm{round}\ (x)$ returns the nearest non-zero integer of x. In this way, it is possible to avoid filtering by setting L_f to zero or smooth the free surface record and the kinematics solution by $L_f{=}1, 2, \ldots$ which Sobey[2] recommended $L_f{=}1$ for laboratory and field records.

It must be noticed that Δt might be different from input and output and so is the number of nodes within the filter (filter resolution). However, the moving filter width $S{=}2s\Delta t$ will be bounded by the moving window width τ if $L_f{=}1$ is chosen so that $S{\leq}\ \tau$.

Finally, the following recommended values for the method parameters where taken from Sobey[2]

$$\begin{gathered} J = 2\ or\ 3 \\ M_{max} = 8 \\ \tau = 0.1T_z \\ L_f = 0\ or\ 1 \end{gathered} \tag{3. 22}$$

It must be noticed that by selecting $M_{max}{=}8$ the width of the local window can be extended to $t{=}{\pm}\tau$.

4. Method validation on regular waves

In this chapter the LF approximation method is tested for the following 2 regular waves and compared with the results obtained by means of the stretching method of Wheeler.

Table 4. 1. SFWT input parameters for a deep-water wave case and a shallow-water wave case. Both waves are used for LF approximation method validation on regular waves.

Wave	Wave height (m)	Water depth (m)	Wave period (s)	Uniform current (m/s)	Truncation order
Deep	20	100	10	0	10
Shallow	3	5	10	-2	18

In this regard, the free surface time history as well as the theoretical wave kinematics for both deep-water and shallow-water waves are calculated by means of the SFWT with a truncation order of $N=10$ and $N=18$ respectively.

Both waves were also studied by Sobey[2] considering the record segment centred on a crest and extended from the previous crest to the following crest with a discrete input free surface elevation data taken at a time step of Δt_{in}=0.5 s.

For the present method validation an alternative zero crossing analysis is inspected combining both zero-down and zero-up crossings and which will lead to half individual wave periods. In this regard, zero crossing analysis appears to be a major issue since it will determine the local window width τ. Therefore, it must be said that isolated difficulties in wave kinematics prediction are mainly found at wave trough when it is particularly flat and changes in η and $\partial\eta/\partial t$–values are rather small within the local window so that a wider window is pertinent, which can be achieved using the combination of both zero-down and zero-up crossings.

Furthermore, no filtering is decided since the free surface elevation is considered to be known quite precisely without error bands so that L_f is set to zero for both deep-water and shallow-water waves. In the same way, neither spectrum smoothing nor cut-off filtering is taken into account for the Wheeler stretching method.

With regard to problem-solving, the Levenberg-Marquardt method presented in the previous chapter with bound constraints on the solution has been chosen as regular solver.

The obtained results are presented by means of four plots. First plot, located at the up-left side corresponds to the free surface elevation record segment (continuous black line) and the discrete input free surface data (black markers). Second plot, located at the up-right side corresponds to the horizontal velocity predicted at the free surface. Third plot, located at the down-left side corresponds to the vertical velocity predicted at the free surface. Fourth plot, located at the down-right side corresponds to the horizontal acceleration predicted at the free surface. The blue markers are predicted kinematics of the LF approximation method, the red markers are predicted kinematics of the Wheeler stretching method and the continuous black lines are the theoretical kinematics predicted by the SFWT.

Comparison of the results between the LF and the Wheeler stretching predictions is made through the Root Mean Squared Error (RMSE) defined as:

$$RMSE(y) = \sqrt{\frac{\sum_{i=1}^{N_{out}} \left(y_i^{SFWT} - y_i^{predicted}\right)^2}{N_{out}}} \quad (4.\ 1)$$

Where y_i is the assessed kinematic variable at t_i and N_{out} is the total number of output nodes.

Besides, comparison is further studied by means of a histogram of the relative error $\left|y_i^{SFWT} - y_i^{predicted}\right|/RMSE(y)$ for each kinematic variable along with the corresponding cumulative distribution of the relative error, where $|x|$ is the absolute value of x.

Moreover, velocities are shown along depth and time through a vector plot. The velocity vectors (u, w) are plotted by means of arrows in which u and w are scaled by a factor of 0.03. The vertical and horizontal axes are represented in dimensionless form by z/h and t/T=10s.

The LF approximation method input parameters used for studying the deep-water wave are shown in Table 4. 2. It must be said, that they are the same as in Sobey[2].

Table 4. 2. LF approximation method input parameters for the study of the deep-water wave.

		Deep		
Δt_{out} **(s)**	J	M_{max}	L_f	τ
0.5	2	8	0	$0.1T_z$

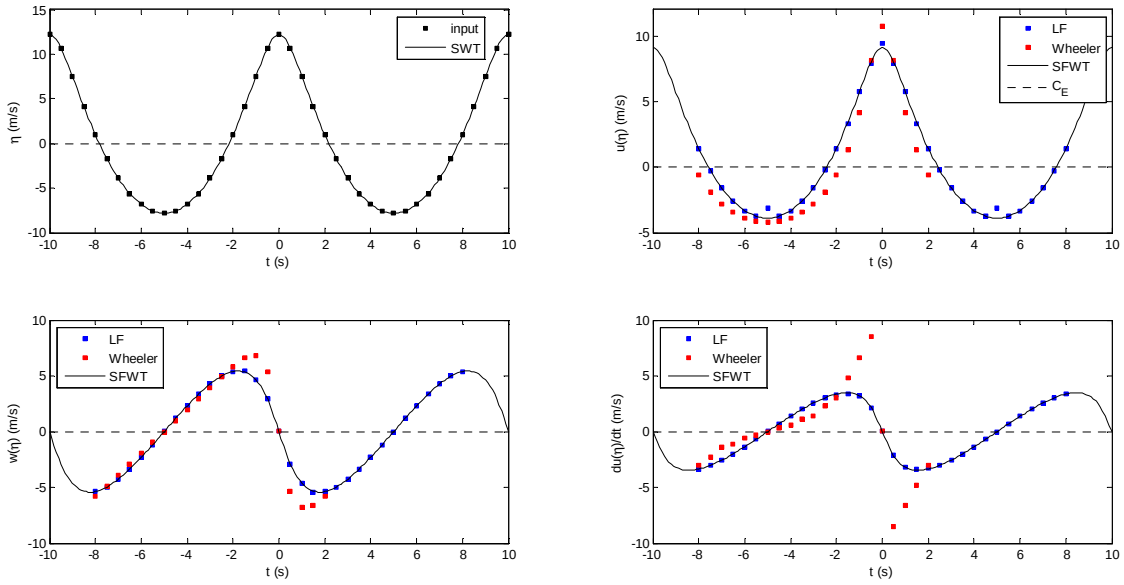

Fig.4. 1. Theoretical SFWT, LF and Wheeler stretching kinematics predictions at the free surface for the deep-water wave.

Fig.4. 1 shows that the LF predictions match the theoretical kinematics obtained by the SFWT with an isolated disagreement at the wave trough. Regarding the stretching method of Wheeler, difficulties in kinematics prediction at the free surface are apparent all along, especially between the zero crossing regions and the wave crest where the magnitude of the horizontal acceleration tends to increase exponentially.

The calculated RMSE–values of the predicted kinematics for both the LF approximation method and the Wheeler stretching method taking into account equation (4. 1) and the discrete data from Fig.4. 1 are reported in the following table:

Table 4. 3. Calculated RMSE of the horizontal velocity, vertical velocity and horizontal acceleration for the deep-water wave taking into account LF and Wheeler stretching kinematics predictions at the free surface.

	Deep	
	LF	**Wheeler**
RMSE $u(\eta)$ (m/s)	0.1931	1.3788
RMSE $w(\eta)$ (m/s)	0.0266	1.1242
RMSE $du(\eta)/dt$ (m/s^2)	0.0380	2.3309

From Table 4. 3 it can be seen that there is a difference of 1 order of magnitude for the horizontal velocity and even 2 orders of magnitude for the vertical velocity and horizontal acceleration between the RMSE obtained by the LF predictions and the RMSE obtained by the Wheeler stretching predictions. Therefore, it makes noticeable that the stretching method of Wheeler has significant difficulties when predicting kinematics at the free surface for such nonlinear deep-water wave. On the other hand, the LF approximation method provides satisfactory kinematics prediction at the free surface, even close to the wave crest and zero crossing regions where velocities and accelerations reach their largest values.

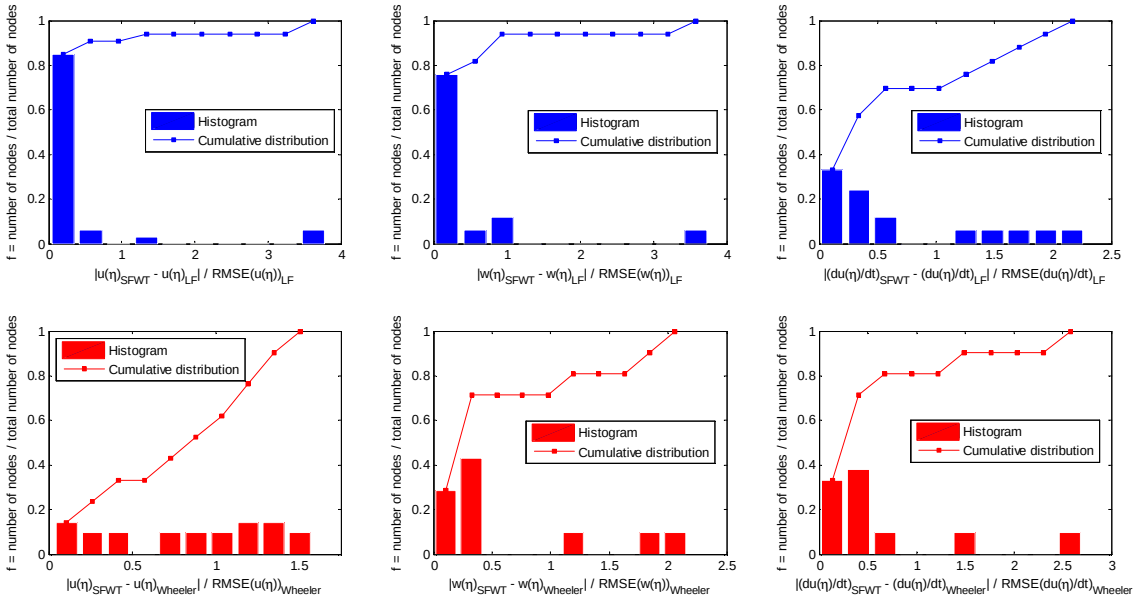

Fig.4. 2. Histogram and cumulative distribution of the relative error of both LF approximation and Wheeler stretching kinematics predictions at the free surface for the deep-water wave.

Fig.4. 2 shows that more than 80% of the nodes for both the horizontal and vertical velocity predicted by the LF approximation method yield errors smaller than half of the calculated RMSE so that larger errors are rather isolated corresponding to less than 20% of the nodes. The histogram of the relative error for the LF horizontal velocity prediction clearly shows that the maximum error of nearly 4 times the calculated RMSE is just produced at the wave trough.

Furthermore, Fig.4. 2 shows that around 70% of the nodes for the vertical velocity and horizontal acceleration predicted by the Wheeler stretching method lead to errors smaller than half of the calculated RMSE and so as it was previously said the largest errors for vertical

velocity and horizontal acceleration are isolated and located between the zero crossing regions and the wave crest (Fig.4. 1) with the maximum error being 2 and 2.5 times the RMSE for the vertical velocity and horizontal acceleration respectively. On the other hand, solely 50% of the nodes for the horizontal velocity predicted by the Wheeler stretching method are smaller than the calculated RMSE though it can be seen that 1.5 times the RMSE is not exceeded at any node.

The next figure shows the velocity distribution along depth at different instants of time regarding both the LF approximation method and the stretching method of Wheeler for the studied deep-water wave.

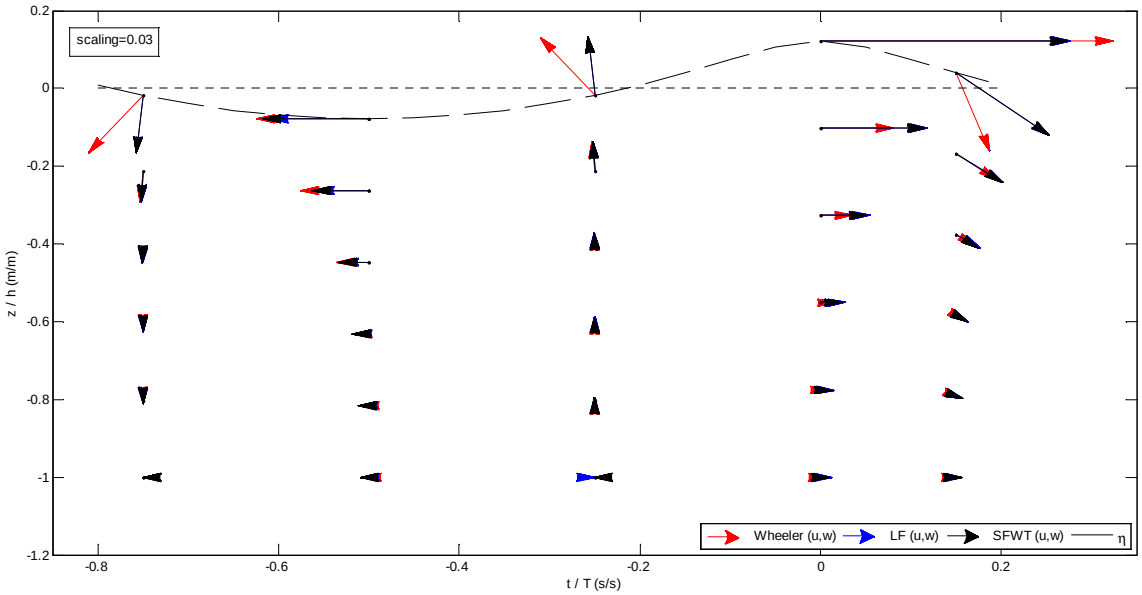

Fig.4. 3. Theoretical SFWT, LF and Wheeler stretching velocity predictions along depth and throughout time for the deep-water wave.

Fig.4. 3 shows a perfect match between velocities predicted along depth by the LF approximation method and the SFWT. However, some errors can be seen at wave trough throughout depth and close to the zero-up crossing region at the bottom although the velocity is nearly zero at this location and for this instant of time. On the other hand, the stretching method of Wheeler overestimates the magnitude of the velocity all along the free surface and changes in the velocity direction nearby the zero-down and up crossing at the free surface are visible. Nevertheless, velocities predicted along depth by the Wheeler stretching method have a good agreement with respect to the theoretical velocities predicted by the SFWT showing that main difficulties in velocity prediction for the Wheeler stretching method are found at the free surface.

The LF approximation method input parameters used for studying the shallow-water wave are shown in Table 4. 4. It must be said, that they are the same as in Sobey[2].

Table 4. 4. LF approximation method input parameters for the study of the shallow-water wave.

Shallow				
Δt_{out} **(s)**	J	M_{max}	L_f	τ
0.5	3	8	0	$0.1T_z$

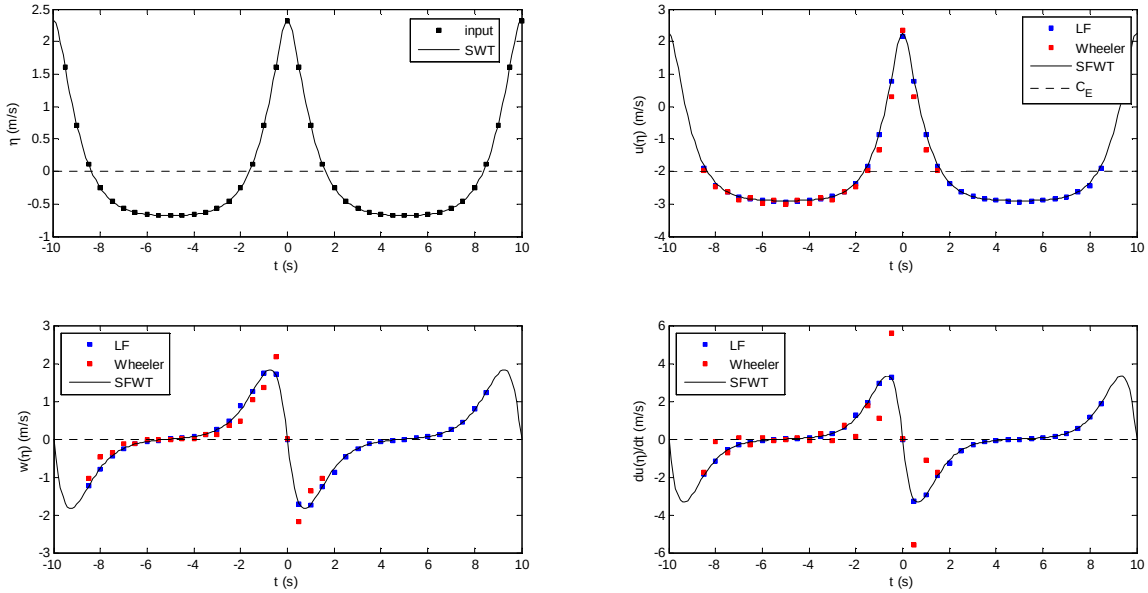

Fig.4. 4. Theoretical SFWT, LF and Wheeler stretching kinematics predictions at the free surface for the shallow-water wave.

For the shallow-water wave $J=3$ is required so as to achieve satisfactory results whereas the rest of the LF parameters reported in Table 4. 4 are the same than for the deep-water wave in Table 4. 2.

Fig.4. 4 shows again perfect agreement between the LF kinematics prediction and the theoretical SFWT kinematics prediction, even at the wave trough where LF horizontal velocity prediction failed for the deep-water wave.

On the other hand, Fig.4. 4 shows oscillations in Wheeler stretching kinematics prediction besides disagreement at the zero crossing regions and the crest side of the profile, which was also seen for the deep-water wave case.

The calculated RMSE–values of the predicted kinematics for both the LF approximation method and the Wheeler stretching method taking into account equation (4. 1) and the discrete data from Fig.4. 4 are reported in the following table:

Table 4. 5. Calculated RMSE of the horizontal velocity, vertical velocity and horizontal acceleration for the shallow-water wave taking into account LF and Wheeler stretching kinematics predictions at the free surface.

	Shallow	
	LF	**Wheeler**
RMSE $u(\eta)$ (m/s)	0.0413	0.2626
RMSE $w(\eta)$ (m/s)	0.0253	0.2295
RMSE $du(\eta)/dt$ (m/s^2)	0.0504	0.9900

From Table 4. 5 it can be seen that there is a difference of 1 order of magnitude between the RMSE obtained by the LF predictions and the RMSE obtained by the Wheeler stretching predictions.

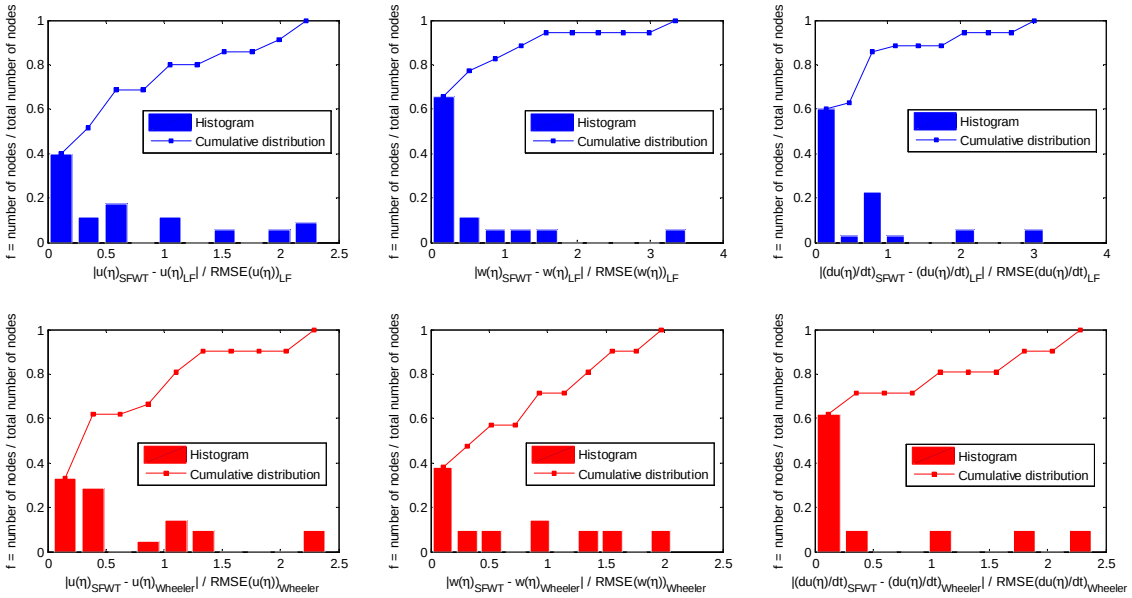

Fig.4. 5. Histogram and cumulative distribution of the relative error of both LF approximation and Wheeler stretching kinematics predictions at the free surface for the shallow-water wave.

The histogram of the relative error for both the LF predictions and the Wheeler stretching predictions shows that larger errors than the calculated RMSE are rather isolated.

Besides, it is noticed that LF kinematics prediction yields errors smaller than half of the calculated RMSE for more than 50% of the nodes.

The next figure shows the velocity distribution along depth at different instants of time regarding both the LF approximation method and the stretching method of Wheeler for the studied shallow-water wave.

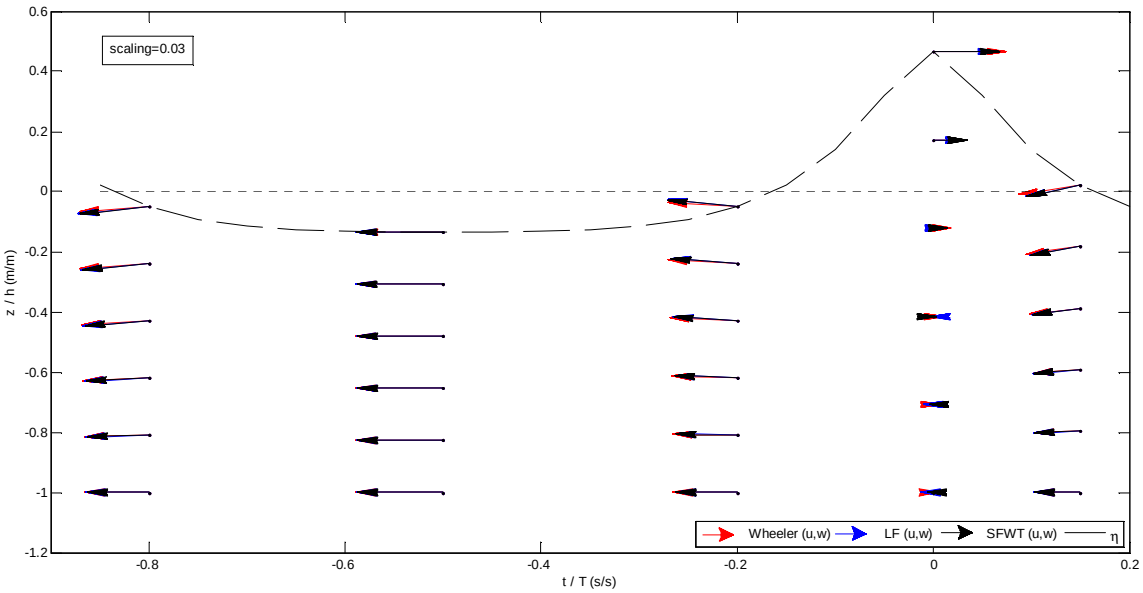

Fig.4. 6. Theoretical SFWT, LF and Wheeler stretching velocity predictions along depth and throughout time for the shallow-water wave.

Fig.4. 6 shows again a perfect match between velocities predicted along depth by the LF approximation method and the SFWT. On the other hand, minor problems in velocity predictions along depth are observed below the wave crest where the LF approximation method predicts the change in velocity direction above what is predicted by the SFWT.

Furthermore, Fig.4. 6 shows a good agreement between the Wheeler stretching velocities prediction at the wave trough and crest as well as close to the zero-up and zero-down crossing regions and throughout depth. Nonetheless, it must be taken into account that major problems in velocities prediction were found nearby the wave crest, which can be seen in Fig.4. 4, but they are not represented in the vector plot from Fig.4. 6.

5. Method validation on irregular waves

In this chapter the LF approximation method is validated on irregular waves and compared with the stretching method of Wheeler through 2 laboratory irregular wave experiments performed in the Ocean Wave Basin at the marine institute (COAST) at Plymouth University. The measured kinematics and the free surface time record for these 2 laboratory experiments were facilitated by Morten M. Jakobsen, Ph.D. Student from Aalborg University. Moreover, a third data set is used which was obtained by digitalization from Sobey[2] corresponding to a wave experiment carried out at the Delft Hydraulics Delta Flume. The significant wave height, water depth, peak period and measured uniform current for all 3 data sets are reported in the following table:

Table 5. 1. Significant wave height and peak period obtained from wave variance spectrum of Plymouth laboratory measurements and Delft Hydraulics Delta Flume experiment, which was reported from Sobey[2]. Furthermore, water depth and uniform current are reported, which are inputs of the LF approximation method and the stretching method of Wheeler.

Id	Significant wave height (m)	Water depth (m)	Peak period (s)	Uniform current (m/s)
Plymouth A1	0.14	2.97	1.98	0.00
Plymouth B4	0.38	2.97	2.63	0.00
Delft Hydraulics Delta Flume	0.80	5.00	6.00	-0.09

The measured kinematics and the free surface were recorded at a time step of Δt_{in}=0.008s for the Plymouth laboratory experiments and the decided input time step for the digitalized wave from Sobey[2] was: Δt_{in}=0.05s.

For the present method validation the alternative zero crossing analysis involving the combination of both zero-up and zero-down crossings taken into account in the previous chapter is used as standard.

Filtering is decided following the recommendations given by Sobey[2] and so setting the parameter L_f=1 for laboratory measurements. In this regard, it is willing to reduce the effect of error bands in the free surface time measurements.

In the same way, spectrum smoothing and cut-off filtering, disregarding frequencies smaller than 1/3 the peak frequency and frequencies bigger than 3 times the peak frequency, is taken into account for the stretching method of Wheeler. The strategy adopted in order to smooth the spectrum was closely related to the filtering procedure followed for the LF approximation method. Thereby, the resulting spectrum is subjected to a moving average filter which its half width correspond to $s=L_f \text{ round } ((\tau_f/\ \Delta f-1)/2)$, where $\tau_f=0.1(3f_p-1/3f_p)$, f_p is the peak period of the non-smoothed spectrum and Δf is the frequency step increment. Besides, the studied record segment for both Plymouth laboratory measurements was split into several subseries each in order to prevent an excess of smoothing and obtain a more accurate kinematics prediction by the stretching method of Wheeler, taking into account that $\Delta f=1/T$,

where T is the time comprised between the first and the last zero-down crossing of the subseries.

With regard to problem-solving, the Levenberg-Marquardt method with bound constraints on the solution has been chosen as the standard solver.

The representation of the results is the same as in method validation on regular waves with the blue markers identifying the LF kinematics prediction, the red markers identifying the Wheeler stretching kinematics prediction and the continuous lines identifying the measured kinematics. On the other hand, kinematics was measured at z=–0.33m for Plymouth data and at z=–1.75m for Delft Hydraulics Delta Flume data and so kinematics are predicted at according depth.

Comparison of the results between the LF and the Wheeler stretching predictions is made through the Root Mean Squared Error (RMSE) defined as:

$$RMSE(y) = \sqrt{\frac{\sum_{i=1}^{N_{out}} \left(y_i^{measured} - y_i^{predicted}\right)^2}{N_{out}}} \tag{5. 1}$$

Where y_i is the assessed kinematic variable at t_i and N_{out} is the total number of output nodes.

Besides, comparison is further studied by means of a histogram of the relative error $\left|y_i^{SFWT} - y_i^{measured}\right| / RMSE(y)$ for each kinematic variable along with the corresponding cumulative distribution of the relative error.

Moreover, velocities are shown along depth and time through a vector plot. The velocity vectors (u, w) are plotted by means of arrows taking into account the same scaling factor for u and w. The vertical and horizontal axes are represented in dimensionless form by z/h and $t/$ (duration of the subseries).

From the available Plymouth A1 data (Fig.5. 1) the record segment from 19s until 48s is chosen for analysis.

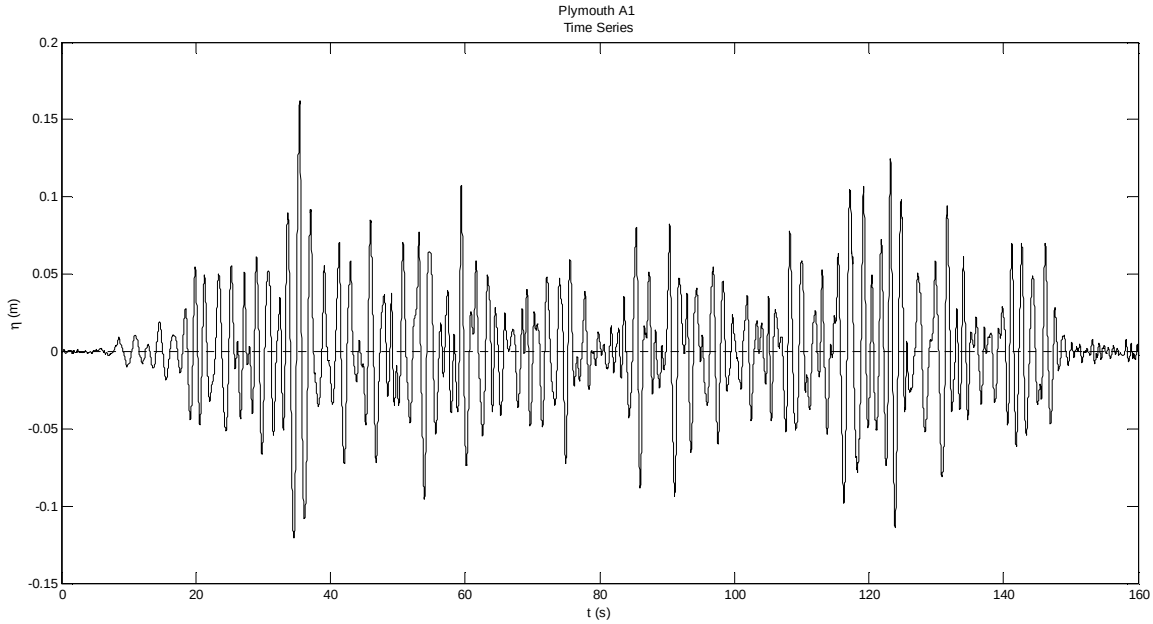

Fig.5. 1. Plymouth A1 experiment free surface elevation time series. The studied record segment is comprised between 19s until 48s.

Besides, 3 subseries were established corresponding to 19s – 29.5s, 28.5s – 39s and 36s – 48s in which spectrum smoothing and cut-off filtering were taken into account for each subseries when predicting kinematics by the stretching method of Wheeler.

The LF approximation method input parameters used for studying the Plymouth A1 record segment are shown in Table 5. 2.

Table 5. 2. LF approximation method input parameters for the study of Plymouth A1 irregular wave experiment from 19s until 48s.

Plymouth A1				
Δt_{out} **(s)**	J	M_{max}	L_f	τ
0.0667	3	8	1	$0.1T_z$

From Fig.5. 2 similar kinematics prediction can be seen when using both the LF approximation method and the stretching method of Wheeler. Besides, agreement with respect to the measured kinematics is generally good for both methods.

Nevertheless, isolated difficulties in LF vertical velocity prediction are found within 3 small individual waves (i.e. short zero-crossing period and small zero-crossing amplitude), 2 found within 25s – 29s and 1 within 43s – 45s. Furthermore, some oscillations in LF vertical velocity prediction are observed. In this regard, no significant improvement was seen neither reducing nor increasing the truncation order J.

On the other hand, the stretching method of Wheeler is observed to overestimate the magnitude of the vertical velocity within the zero-down crossing region at around 29s though it is associated with the starting time of the subseries 28.5s – 39s, as well as within the zero-down crossing regions at 35s (corresponding to the largest amplitude individual wave) and also just right after.

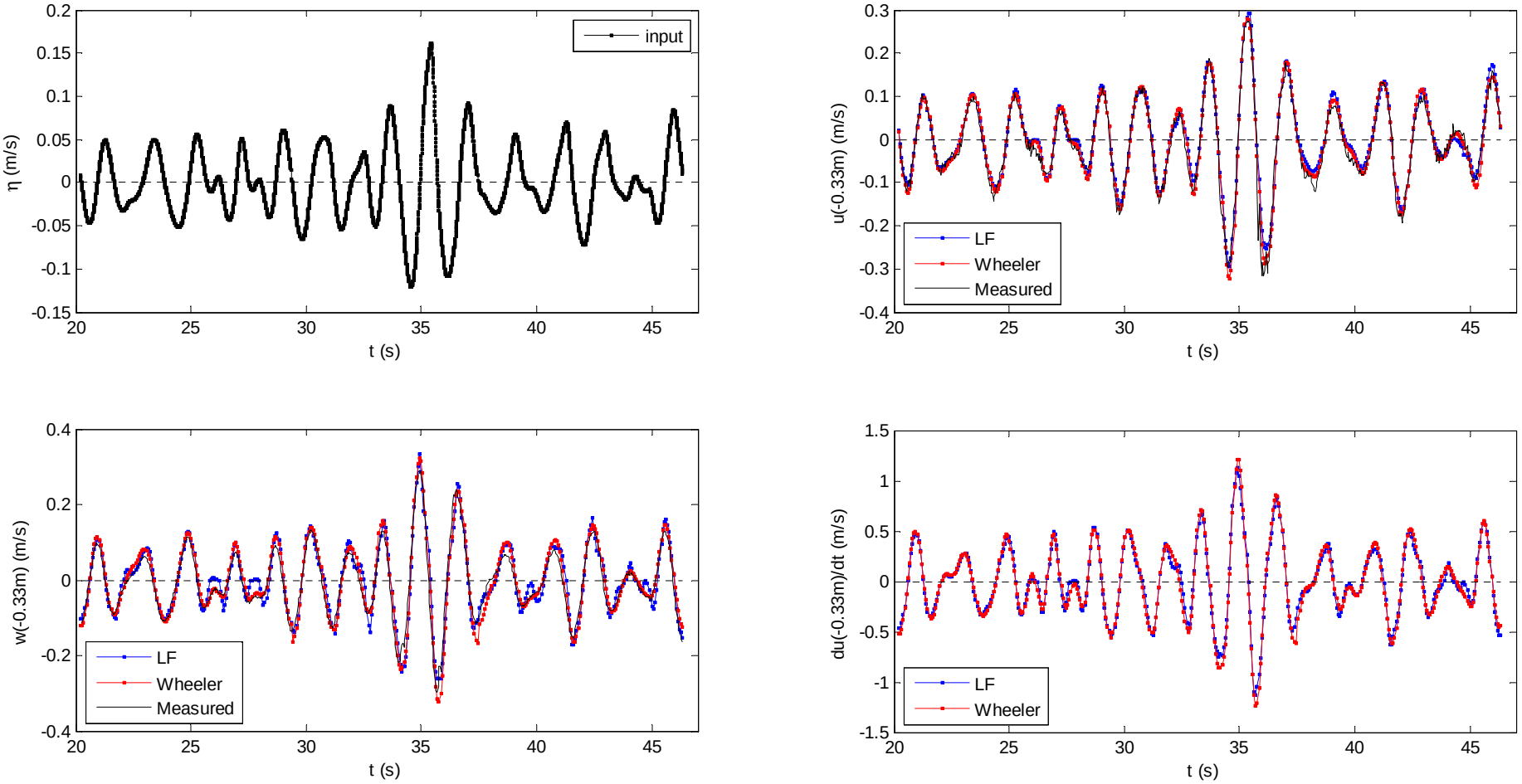

Fig.5. 2. LF and Wheeler stretching kinematics predictions at z=–0.33m for the Plymouth A1 irregular wave experiment from 19s until 48s.

It must be said that agreement is good for horizontal velocity prediction using both methods.

The calculated RMSE–values of the predicted kinematics for both the LF approximation method and the Wheeler stretching method taking into account equation (5. 1) and the discrete data from Fig.5. 2 are reported in the following table:

Table 5. 3. Calculated RMSE of the horizontal and vertical velocity for the Plymouth A1 irregular wave experiment from 19s until 48s taking into account LF and Wheeler stretching horizontal and vertical velocity predictions at z=–0.33m.

Plymouth A1		
	LF	**Wheeler**
RMSE u(–0.33m) (m/s)	0.0194	0.0167
RMSE w(–0.33m) (m/s)	0.0290	0.0249

RMSE–values shows again that kinematics prediction is similar when using both methods, yielding a RMSE of approximately 10% of the maximum measured horizontal and vertical velocity. Besides, it can be seen that the RMSE of the vertical velocity is bigger than the RMSE of the horizontal velocity for both methods.

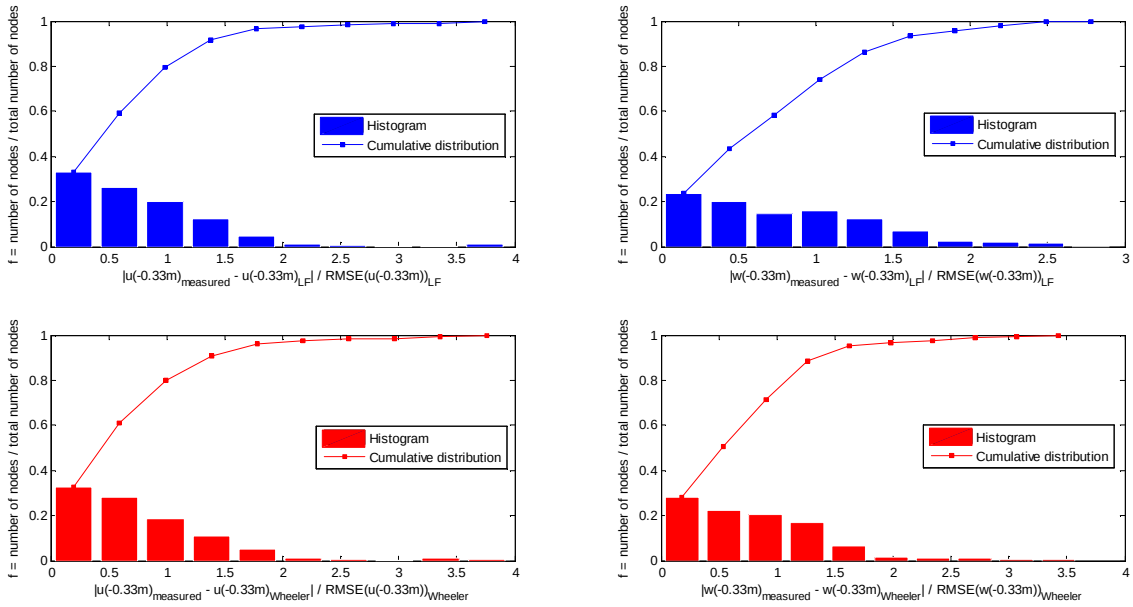

Fig.5. 3. Histogram and cumulative distribution of the relative error of both LF approximation and Wheeler stretching horizontal and vertical velocity predictions at z=–0.33m for the Plymouth A1 irregular wave experiment from 19s until 48s.

Fig.5. 3 shows that the relative error distribution is nearly the same for both methods with small errors making up most of the total amount of nodes. Thereby, both LF approximation and Wheeler stretching velocity prediction does not exceed the calculated RMSE in at least 80% of the nodes.

The next figure shows the velocity distribution along depth at different instants of time regarding both the LF approximation method and the stretching method of Wheeler for the studied 19s – 48s record segment from Plymouth A1 laboratory experiment.

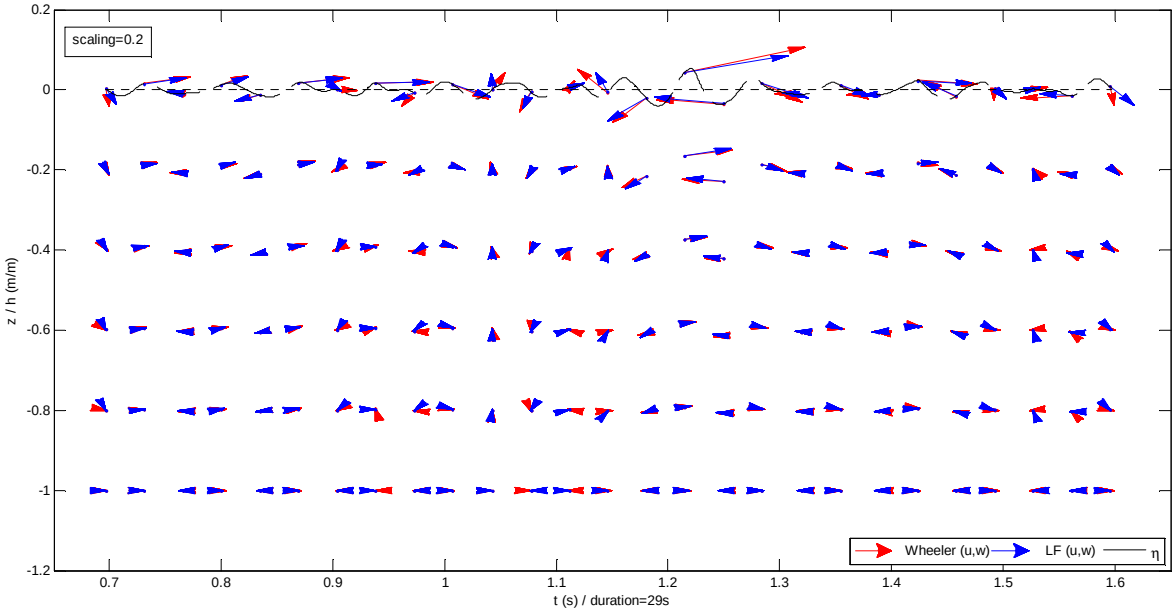

Fig.5. 4. LF and Wheeler stretching velocity predictions along depth and throughout time for the Plymouth A1 irregular wave experiment from 19s until 48s.

Velocity predictions along depth are represented in Fig.5. 4. It is then visible that the Wheeler stretching method usually predicts larger velocities than the LF approximation method all along the free surface. Moreover, disagreement in velocity direction is observed throughout depth between both methods.

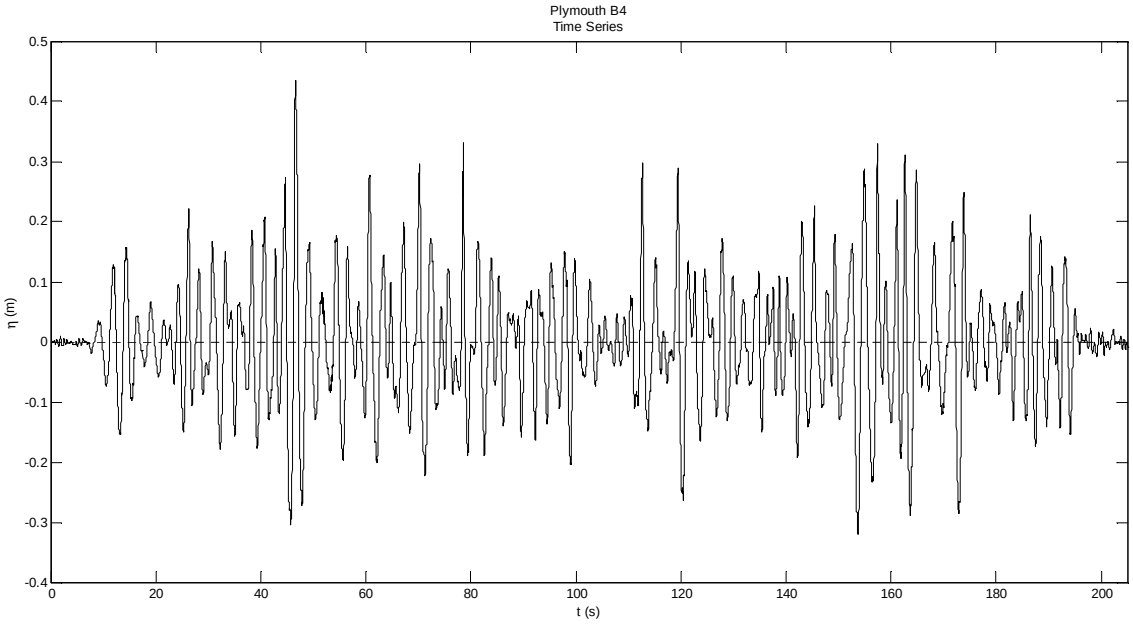

Fig.5. 5. Plymouth B4 experiment free surface elevation time series. The studied record segment is comprised between 8s until 32s.

From the available Plymouth B4 data (Fig.5. 5) the record segment from 8s until 32s is chosen for analysis. The record segment corresponding to 40s – 50s shows the largest individual wave height so that it is of interest for the current method validation, nonetheless the ADV device

was seen to fail when the recorded free surface elevation was larger than approximately $\pm$ 0.25m and so it was not possible to study.

Besides, 2 subseries were established corresponding to 8s – 25s and 24s – 32s in which spectrum smoothing and cut-off filtering were taken into account for each subseries when predicting kinematics by the stretching method of Wheeler.

The LF approximation method input parameters used for studying the Plymouth B4 analysed record segment are shown in Table 5. 4.

Table 5. 4. LF approximation method input parameters for the study of Plymouth B4 irregular wave experiment from 8s until 32s.

Plymouth B4				
Δt_{out} **(s)**	J	M_{max}	L_f	τ
0.0667	3	8	1	$0.1T_z$

Fig.5. 6 shows again similar kinematics prediction when using both the LF approximation method and the stretching method of Wheeler. Overall, there is a good agreement between predicted and measured kinematics regardless of the utilized method.

With regard to LF vertical velocity prediction, it is seen to have an excellent agreement with measurements but for isolated errors in the zero-up crossing region at approximately 28s and in the zero-down crossing region at approximately 25s though it is associated with the starting time of the subseries 24s – 32s. On the other hand, LF horizontal velocity prediction presents rather more disagreements with measurements than for the vertical velocity prediction. In this way, errors are mainly found at trough regions where the magnitude of the velocity is underestimated.

Regarding Wheeler stretching vertical velocity prediction, it shows overestimation of the velocity magnitude in both zero-down crossing and zero-up crossing regions throughout the whole record duration. On the other hand, Wheeler stretching horizontal velocity prediction shows overestimation of the velocity magnitude in wave crest region at approximately 12s and 14s as well as in wave trough region at approximately 15s, 18s, 25s and 30s.

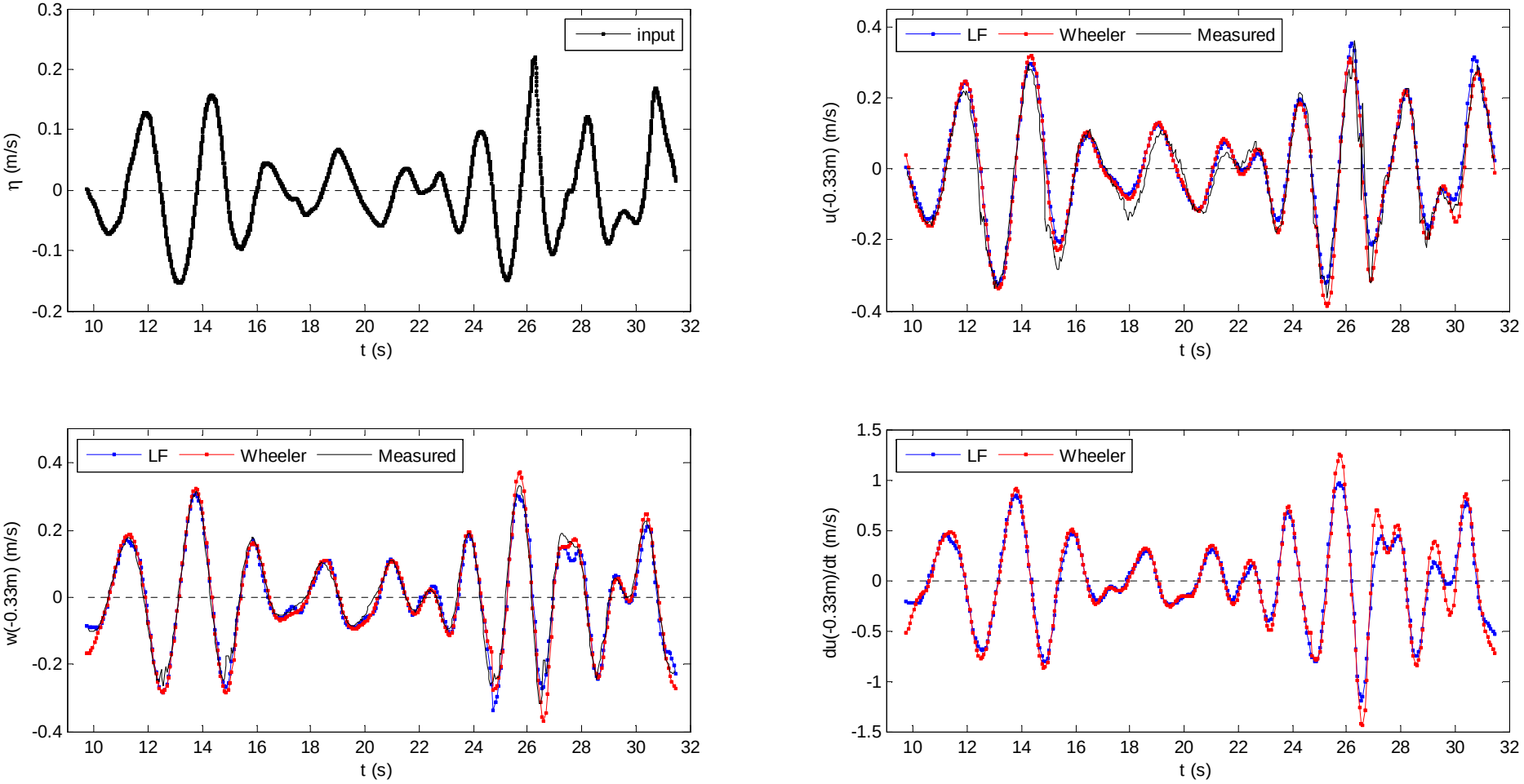

Fig.5. 6. LF and Wheeler stretching kinematics predictions at z=–0.33m for the Plymouth B4 irregular wave experiment from 8s until 32s.

The calculated RMSE–values of the predicted kinematics for both the LF approximation method and the Wheeler stretching method taking into account equation (5. 1) and the discrete data from Fig.5. 6 are reported in the following table:

Table 5. 5. Calculated RMSE of the horizontal and vertical velocity for the Plymouth B4 irregular wave experiment from 8s until 32s taking into account LF and Wheeler stretching horizontal and vertical velocity predictions at z=–0.33m.

Plymouth B4		
	LF	**Wheeler**
RMSE u(–0.33m) (m/s)	0.0336	0.0341
RMSE w(–0.33m) (m/s)	0.0268	0.0308

RMSE–values shows again that kinematics prediction is similar when using both methods, yielding a RMSE of approximately 10% of the maximum measured horizontal and vertical velocity. Moreover, unlike Plymouth A1 the largest RMSE is calculated from the horizontal velocity prediction.

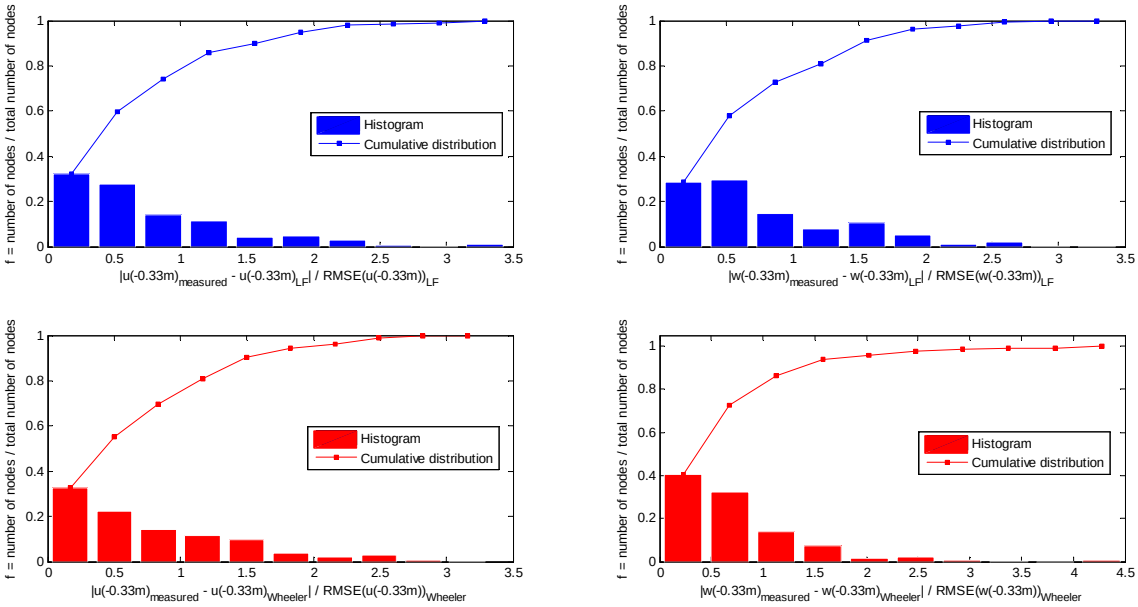

Fig.5. 7. Histogram and cumulative distribution of the relative error of both LF approximation and Wheeler stretching horizontal and vertical velocity predictions at z=–0.33m for the Plymouth B4 irregular wave experiment from 8s until 32s.

The relative error is seen to be rapidly accumulated for both methods so that the calculated RMSE is not exceeded in around 80% of the total number of nodes in either case.

The next figure shows the velocity distribution along depth at different instants of time regarding both the LF approximation method and the stretching method of Wheeler for the studied 8s – 32s record segment from Plymouth B4 laboratory experiment.

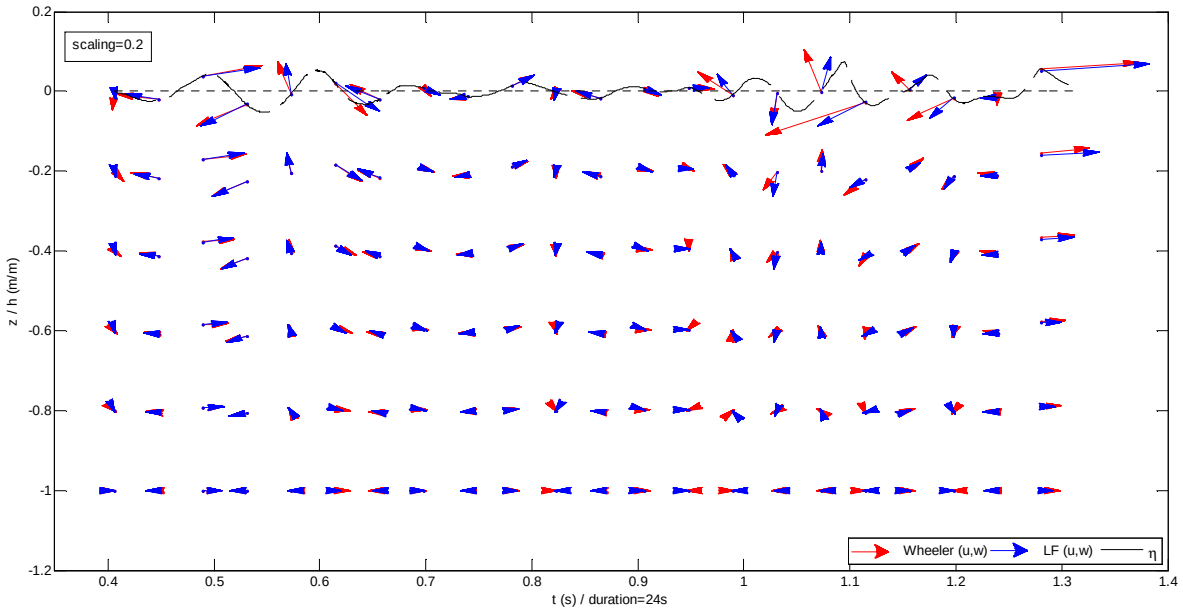

Fig.5. 8. LF and Wheeler stretching velocity predictions along depth and throughout time for the Plymouth B4 irregular wave experiment from 8s until 32s.

From Fig.5. 8 it can be seen that disagreement in predicted velocity direction throughout depth is mainly found at the end of the studied record segment where kinematics are rather more extreme. Furthermore, it can be seen that Wheeler stretching velocity prediction slightly tends to be larger than LF velocity prediction along the free surface.

The next assessed record segment, which was obtained by digitalization from Sobey[2] corresponding to a wave laboratory experiment carried out at the Delft Hydraulics Delta Flume, was thought to be worth studying since measured kinematics are indeed more extreme than for Plymouth laboratory experiments.

Furthermore, it must be said that there was no need to split the analysed record segment in several subseries for Wheeler stretching method though 2 different zero crossing analysis had to be performed in order to span the whole register. In this way, zero-down crossing analysis was done to predict kinematics along the first wave trough region (i.e. 54s – 58s) and zero-up crossing analysis for the rest of the record.

Table 5. 6. LF approximation method input parameters for the study of Delft Hydraulics Delta flume irregular wave experiment reported in Sobey[2].

Delft Hydraulics Delta Flume				
Δt_{out} **(s)**	J	M_{max}	L_f	τ
0.1667	3	8	1	$0.1T_z$

It must be said that LF method parameters were chosen the same as in Sobey[2].

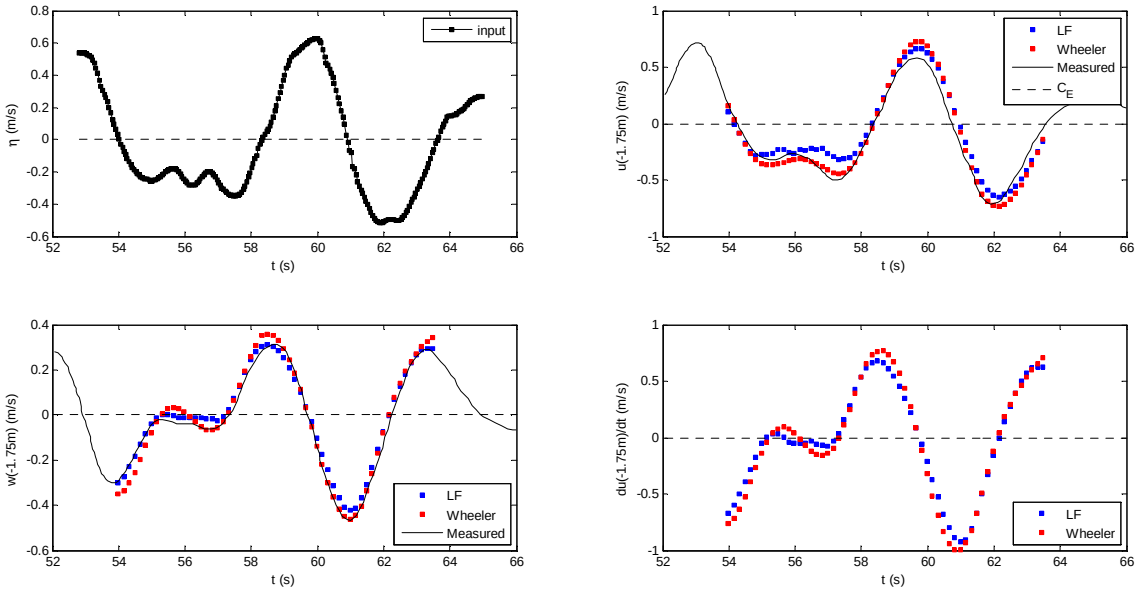

Fig.5. 9. LF and Wheeler stretching kinematics predictions at z=–1.75m for the Delft Hydraulics Delta Flume irregular wave experiment.

From Fig.5. 9 it is seen an excellent agreement between the Wheeler stretching horizontal velocity prediction and measurements within the trough region from 54s – 58s unlike the LF approximation method which is less accurate within this time segment. On the other hand, LF horizontal velocity prediction has a better agreement with measurements than what does Wheeler stretching in the wave crest region at approximately 59s.

With regard to the measured vertical velocity, agreement with LF vertical velocity prediction is excellent. On the other hand, Wheeler stretching method reveals slight difficulties for vertical velocity prediction in the 2 zero-up crossing regions of the profile.

The calculated RMSE–values of the predicted kinematics for both the LF approximation method and the Wheeler stretching method taking into account equation (5. 1) and the discrete data from Fig.5. 9 are reported in the following table:

Table 5. 7. Calculated RMSE of the horizontal and vertical velocity for the Delft Hydraulics Delta Flume irregular wave experiment taking into account LF and Wheeler stretching horizontal and vertical velocity predictions at z=–1.75m.

Delft Hydraulics Delta Flume		
	LF	**Wheeler**
RMSE u(–1.75m) (m/s)	0.1057	0.0920
RMSE w(–1.75m) (m/s)	0.0338	0.0387

The same order of magnitude for the calculated RMSE is observed in Table 5. 7 in which the RMSE of the vertical velocity and horizontal velocity constitute 10% of the maximum measured vertical velocity and around 15% of the maximum measured horizontal velocity respectively.

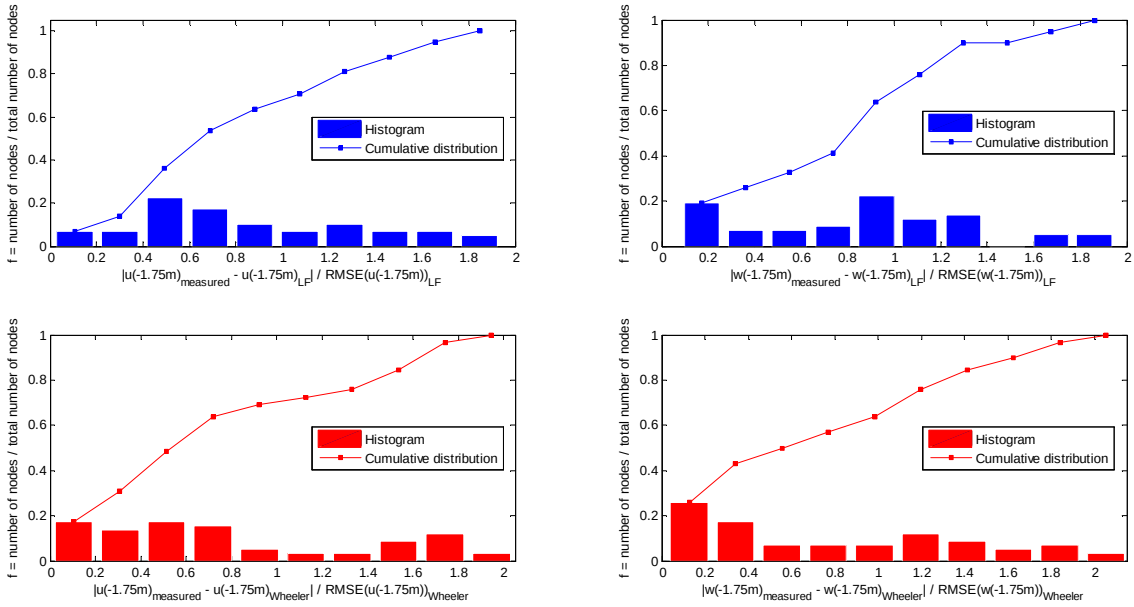

Fig.5. 10. Histogram and cumulative distribution of the relative error of both LF approximation and Wheeler stretching horizontal and vertical velocity predictions at z=–1.75m for the Delft Hydraulics Delta Flume irregular wave experiment.

Unlike what was observed for Plymouth results, the range of the relative error is narrower being up-bounded by 2 times the calculated RMSE. However, this narrower range is continuously distributed among all the nodes so that the RMSE is accumulated by approximately 60% of the nodes. Therefore, larger errors than RMSE are not isolated and so they tend to be widespread.

The next figure shows the velocity distribution along depth at different instants of time regarding both the LF approximation method and the stretching method of Wheeler for the studied record segment from Delft Hydraulics Delta flume laboratory experiment.

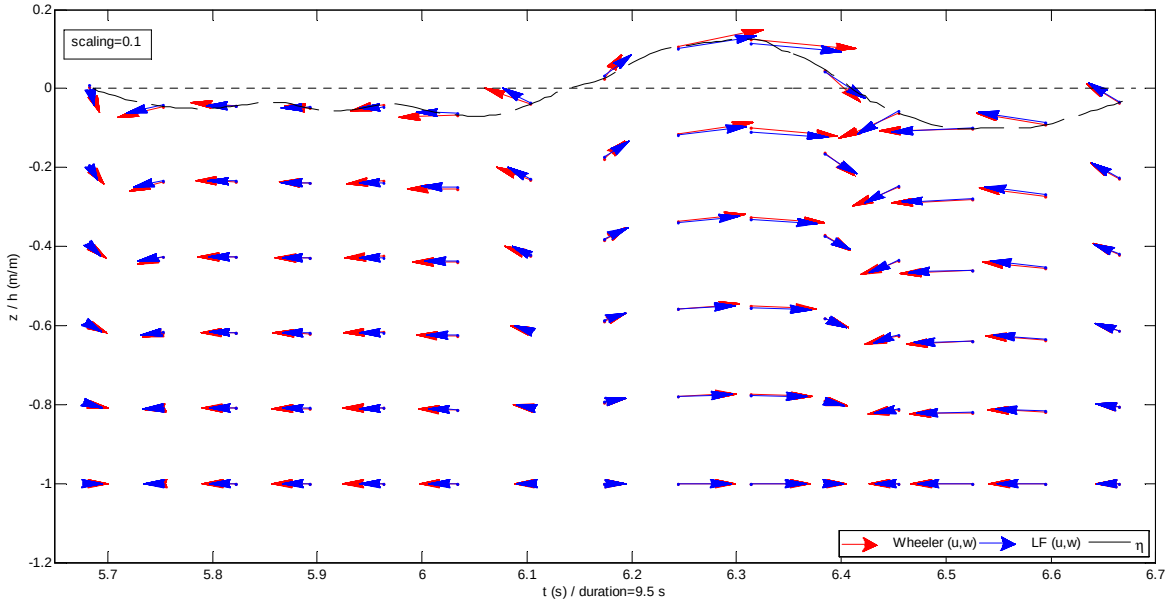

Fig.5. 11. LF and Wheeler stretching velocity predictions along depth and throughout time for the Delft Hydraulics Delta Flume irregular wave experiment.

From Fig.5. 11 a perfect agreement in velocity direction throughout depth is seen between both method predictions. Moreover, Wheeler stretching velocity prediction tends to be larger than LF velocity prediction all along the record duration and throughout depth.

6. Conclusions and perspectives

The implemented Local Fourier approximation method presented by Sobey[2] is a useful tool in order to predict irregular wave kinematics when the free surface time history is available from measurements. Better performance upon irregular wave kinematics prediction compared to other existing methodologies is expected to be found at the free surface where the nonlinear free surface boundary conditions are solved exactly, without the involvement of any empirical transformation such as it is done in the stretching method of Wheeler, but introducing a steady assumption so as to estimate the unknown spatial gradients of the free surface elevation required by the imposition of the kinematic free surface boundary condition. Nevertheless, the wave is assumed locally steady within each established window so that such an assumption will not reach out all along the wave and so being bounded by the decided window width.

The Local Fourier approximation method is a generalization of the well-known Stream Function Wave Theory method, which is widely accepted and used when predicting kinematics of regular waves. Both methods are based on an approximation of the velocity potential and the stream function respectively through a truncated Fourier-series which directly fulfils the field equation and the bottom boundary condition so that problem-solving is based on the imposition of the free surface boundary conditions at exact free surface elevation values. In this way, the Local Fourier approximation method is presented as a local method in which the problem solution is obtained within a narrow moving window unlike the Stream Function Wave Theory in which a unique solution is obtained for the entire regular wave. Since periodicity condition is implicit in the representation of the velocity potential through a Fourier-series, the choice of a local methodology for predicting kinematics of irregular waves appears to be more suitable.

Testing the Local Fourier approximation method with theoretical kinematics at the free surface of regular waves has shown excellent agreement. On the other hand, comparison of predicted kinematics with the stretching method of Wheeler has shown the weaknesses of such methodology when predicting kinematics at the free surface and for markedly nonlinear waves. The difference in kinematics prediction for both methods was concluded by a comparison of the RMSE which revealed a difference of 1 order of magnitude in the least case and which is a consequence of the linear assumption taken into account in the stretching method of Wheeler.

Testing the Local Fourier approximation method with laboratory measurements of irregular wave experiments has shown good agreement with solely minor isolated errors. Moreover, the obtained Wheeler stretching kinematics prediction showed a perfect match with measured kinematics. Analysis of the free surface elevation record suggests that the waves are rather lineal which prevents Wheeler stretching predictions to be inaccurate.

Potential error sources for the Local Fourier approximation method are several and their identification will give information about the capabilities of such methodology.

Numerical errors are readily identified which mainly stem from the numerical solution of the bound constrained nonlinear least squares problem faced in each local window. Thus, 4 methods have been implemented which can accept bound constraints on the solution, in which 2 of them, the Levenberg-Marquardt method and the Trust Region Reflective method, are worth using. In this way, it must be noticed that the Levenberg-Marquardt method is not first thought to accept bound constraints on the solution but it has been conveniently modified to do so, which will unequivocally reduce its efficiency so that the possibility to choose an alternative solver, such as the Trust Region Reflective method, might be advantageous. Moreover, both initial estimates on the iteration and window width are tightly linked with the considered zero crossing analysis. Thus, zero-down crossing analysis, zero-up crossing analysis and zero crossing analysis using a combination of both zero-down and zero-up crossings have been implemented, in which the last is seen to be the most suitable and so it has been used for method validation and set as standard. However, some problems may arise for short-period individual waves in which the combination of zero-down and zero-up crossings will give rise to extremely large initial estimates of both ω_0 and k and consequently leading to undefined or unfeasibly large initial values of the free surface boundary functions and the corresponding Jacobian matrix of the nonlinear least squares problem. Even though short-period individual waves are rare, the problematic might be overcome by use of zero-down or zero-up crossing analysis instead.

Error bands in the input free surface time history is also a major issue that LF approximation method has to cope with. In this way, an average filter is implemented in order to smooth the input free surface record and get smooth temporal gradients. Despite filtering, it is not always sufficient and errors in kinematics prediction may arise which should be considered when analysing the obtained results.

Possible errors in wave kinematics prediction are also associated with the assumptions taken into account in problem formulation. Therefore, the local steady free surface assumption as well as the implicit periodicity condition in the approximated velocity potential is with no doubt a source of errors when predicting kinematics of irregular waves which are by nature unsteady.

After the LF approximation method has been validated on stream function waves and irregular waves from laboratory experiments, promising future work would be focused on method validation on markedly nonlinear irregular waves and irregular waves with extreme asymmetry around the wave crest.

7. References

[1] Thomas Lykke Andersen, Peter Frigaard and Hans F. Burcharth, Lecture notes for the course in water wave mechanics. *Aalborg University, ISSN 1991-7286* (2012): 5-28.

[2] Sobey, R. J., A local Fourier approximation method for irregular wave kinematics. *Applied Ocean Research, 14* (1992): 93-105.

[3] John D. Fenton, Numerical methods for nonlinear waves. *Advances in Coastal and Ocean Engineering, vol. 5 ed. P.L. - F.Liu* (1999): 8-15.

[4] D. Clamond and A. Constantin, Recovery of steady periodic wave profiles from pressure measurements at the bed. *J. Fluid Mech., vol. 714* (2013): 463.

[5] Peter Frigaard, Thomas Lykke Andersen and Morten Møller Jakobsen, Analysis of waves. *Aalborg University ISSN 1901-726X* (2012): 21-35.

[6] Henri P. Gavin, The Levenberg-Marquardt method for nonlinear least squares curve-fitting problems. *Duke University* (2013): 1-4.

[7] K. Madsen, H. B. Nielsen and O. Tingleff, Methods for nonlinear least squares problems. *Technical University of Denmark* (2004): 2-54.

[8] Shidong Shan, A Levenberg-Marquardt method for large-scale bound-constrained nonlinear least-squares. *British Columbia University* (2008): 8-9.

[9] Johnathan M. Bardsley, A bound-constrained Levenberg-Marquardt algorithm for a parameter identification problem in electromagnetics. *University of Montana, Missoula, MT 59812-0864* (2004): 6-13.

[10] Bruce R. Munson, Donald F. Young, Theodore H. Okiishi and Wade W. Huebsch, Fundamental of fluid mechanics. *John Wiley & Sons, Inc., sixth edition, ISBN 978-0470-26284-9*: 269-284.

[11] Ascher H. Shapiro, Film notes for vorticity. *Education Development Center, National Comitee for Fluid Mechanics Films* (1969): 1-4.

[12] Miguel Angel Pascual Iglesias, Teoria de campos escalares y campos vectoriales. *MAPI, Madrid* (2009): 12-13.

Appendix

A.1. Conservation of mass.

Considering an arbitrary fixed volume (CV), the water mass variation with time inside CV must equal the water mass flowing through CV boundaries (CS) per unit time (mass that comes in minus mass that goes out, per unit time) as long as there are no sinks or sources of water mass (Fig. A. 1).

$$\frac{\partial}{\partial t}\begin{pmatrix}\text{Total Water Mass}\\ \text{inside CV}\end{pmatrix} = \begin{matrix}\text{Total Water Mass Flowing}\\ \text{through CS per unit time}\end{matrix} \tag{A. 1}$$

$$\frac{\partial}{\partial t}\left(\int_{CV} \rho \, d\tilde{\forall}\right) = -\int_{CS} \rho(\boldsymbol{V}\cdot\boldsymbol{n})\, dA \tag{A. 2}$$

Where $\text{Mass}=\rho\ (\text{Volume})$, ρ is the water density, $d\tilde{\forall}$ and dA are differentials of volume and area respectively; $\boldsymbol{V}$ is the velocity field and $\boldsymbol{n}$ is the normal vector to CS. Besides, negative sign is set to the right hand side of equation (A. 2) since $\boldsymbol{n}>0$ is decided to point out from CV and so $\boldsymbol{V}\cdot\boldsymbol{n}>0$ corresponds to an outflow and so to a negative water mass variation with time inside CV.

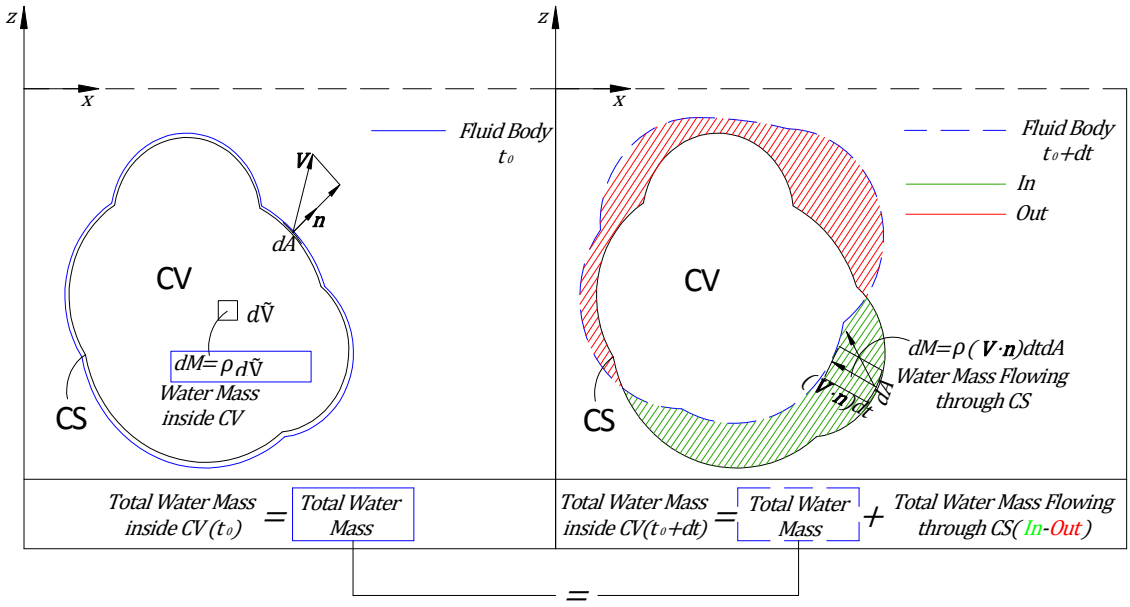

Fig. A. 1. Sketch of how the water mass varies with time inside CV as the fluid body, occupying CV at t_0, interacts with it.

The area integral regarding the water mass flow through CS can be rewritten into the volume integral of CV by means of the divergence theorem:

$$\int_{\text{Surf}} \mathbf{VectorField}\cdot\boldsymbol{n}\, dA = \int_{\text{Vol}} (\boldsymbol{\nabla}\cdot\mathbf{VectorField})\, d\tilde{\forall} \tag{A. 3}$$

$$\int_{CS} \rho(\boldsymbol{V}\cdot\boldsymbol{n})\, dA = \int_{CV} (\boldsymbol{\nabla}\cdot\rho\boldsymbol{V}) d\tilde{\forall} \tag{A. 4}$$

Where $\boldsymbol{\nabla}\cdot$ is the divergence operator, Vol is a volume and Surf is the boundary surface of Vol.

Thus, substituting equation (A. 4) into (A. 2) yields:

$$\int_{CV} \left(\frac{\partial \rho}{\partial t} + \boldsymbol{\nabla} \cdot \rho \boldsymbol{V} \right) d\tilde{\mathrm{V}} = 0 \tag{A. 5}$$

Equation (A. 5) must hold for an arbitrary CV and thus it is just fulfilled when the integrand cancels out.

$$\frac{\partial \rho}{\partial t} + \boldsymbol{\nabla} \cdot \rho \boldsymbol{V} = 0 \tag{A. 6}$$

Equation (A. 6) is the differential form of the so-called continuity equation[10] and is a recurrent equation used in fluid mechanics problems. Since it is given in its differential form, equation (A. 6) must be fulfilled at every point of the problem domain.

Nevertheless, some assumptions according to the studied water-wave mechanics problem can be considered in order to simplify equation (A. 6).

Incompressible fluid is assumed and so time derivative of water density is set to zero and water density can be set out of the divergence operator which yields:

$$\begin{gathered} \boldsymbol{\nabla} \cdot \boldsymbol{V} = 0 \\ \frac{\partial u}{\partial x} + \frac{\partial v}{\partial y} + \frac{\partial w}{\partial z} = 0 \end{gathered} \tag{A. 7}$$

Besides, irrotational flow is assumed. A flow is said to be irrotational if the vorticity field is null at every point:

$$\boldsymbol{\omega} = \left(\frac{\partial v}{\partial z} - \frac{\partial w}{\partial y} \right) \boldsymbol{i} + \left(\frac{\partial w}{\partial x} - \frac{\partial u}{\partial z} \right) \boldsymbol{j} + \left(\frac{\partial u}{\partial y} - \frac{\partial v}{\partial x} \right) \boldsymbol{k} = \boldsymbol{0} \tag{A. 8}$$

Where $\boldsymbol{\omega}$ is the vorticity field, see Appendix A.3.

From equation (A. 8) it can be seen that assuming irrotational flow, $\boldsymbol{\omega}=\boldsymbol{0}$, will provide a relationship between the partial derivatives of the velocity field. Such relationship is guaranteed when the velocity field stems from a scalar potential Φ the so-called velocity potential.[10]

$$\begin{gathered} \boldsymbol{V} = \boldsymbol{\nabla}(\Phi) \\ (u, v, w) = \left(\frac{\partial \Phi}{\partial x}, \frac{\partial \Phi}{\partial y}, \frac{\partial \Phi}{\partial z} \right) \end{gathered} \tag{A. 9}$$

Where $\boldsymbol{\nabla}(\cdot)$ is the gradient operator.

Furthermore, 2D plane flow is assumed (x–z–plane). For such type of flows, the velocity component in transversal direction is considered negligible (y–direction for this problem).

Overall, for an incompressible fluid and plane irrotational flow the mass balance equation can be rewritten substituting equation (A. 9) into equation (A. 7) and disregarding flow in y–direction as follows:

$$\frac{\partial^2 \Phi}{\partial x^2} + \frac{\partial^2 \Phi}{\partial z^2} = 0 \tag{A. 10}$$

Equation (A. 10) is the so-called Laplace's equation and it must be fulfilled at every point of the problem domain. Hence, it is usually called field equation.

A.2. Conservation of linear momentum

Considering an arbitrary fixed volume (CV), the linear momentum ($\boldsymbol{P}$) variation with time inside CV must equal the linear momentum flowing through CV boundaries (CS) per unit time ($\boldsymbol{P}$ that comes in minus $\boldsymbol{P}$ that goes out, per unit time) plus a "force term" (Fig. A. 2).

$$\frac{\partial}{\partial t}\begin{pmatrix}\text{Total } \mathbf{P} \\ \text{inside CV}\end{pmatrix} = \begin{matrix}\text{Total } \mathbf{P} \text{ Flowing} \\ \text{through CS per unit time}\end{matrix} + \text{force} \qquad \text{(A. 11)}$$

Where $\boldsymbol{P}=\boldsymbol{V}$ (Mass).

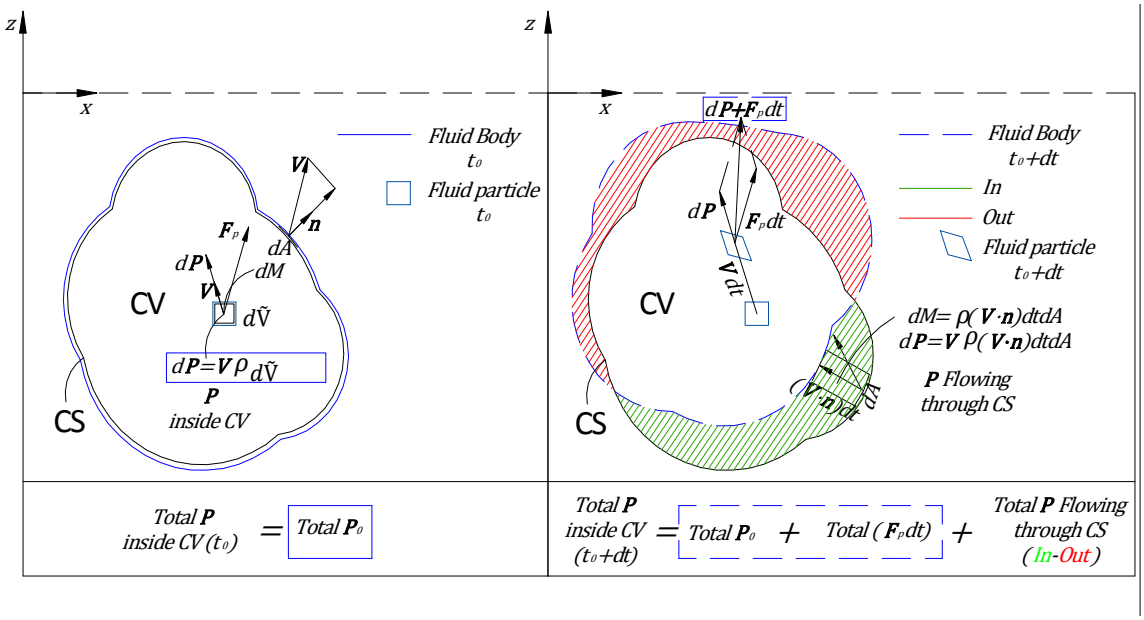

Fig. A. 2. Sketch of how the linear momentum $\boldsymbol{P}$ varies with time inside CV as the fluid body, occupying CV at t_0, interacts with it.

The fluid particles will bring $\boldsymbol{P}$ in and out to CV as they move about, and this is what the "flowing term" from equation (A. 11) denotes.

Furthermore, if a non-null resultant external force $\boldsymbol{F}$ is acting at a certain instant of time t_0 upon the fluid body, which consists of all the fluid particles occupying CV at t_0, such fluid body will experience a change in $\boldsymbol{P}$ per unit time of same magnitude and direction than $\boldsymbol{F}$ (Newton's Second Law). In this regard, this is what the "force term" from equation (A. 11) denotes.

$$\boldsymbol{P}_{Fluid\ Body}(t_0 + dt) = \boldsymbol{P}_{Fluid\ Body}(t_0) + \boldsymbol{F}dt \qquad \text{(A. 12)}$$

From Fig. A. 2, it can be seen that $\boldsymbol{P}$ inside CV equals $\boldsymbol{P}$ of the fluid body at t_0 (left side of Fig. A. 2). After a small time increment though, part of $\boldsymbol{P}$ exits from CV (red region) and extra $\boldsymbol{P}$ steps in CV (green region). Besides, $\boldsymbol{P}$ of the fluid body (region enclosed by dashed blue line)

changes according to Newton's Second Law (equation (A. 12)). Therefore, the linear momentum equation turns out to be:[10]

$$\frac{\partial}{\partial t}\left(\int_{CV} \boldsymbol{V}\rho \, d\tilde{\forall}\right) = -\int_{CS} \boldsymbol{V}\rho(\boldsymbol{V}\cdot\boldsymbol{n}) \, dA + \boldsymbol{F} \qquad \text{(A. 13)}$$

Hereafter, the "force term" will be developed under the assumption of inviscid flow. A flow is said to be inviscid if the shearing stresses are negligible.[10] Therefore, Pascal's law can be taken into account, which states that "the pressure at a point in a fluid at rest, or in motion, is independent of direction as long as there are no shearing stresses present".

Overall, it can be said, that for an inviscid flow, the fluid body occupying CV at t_0, will be subjected to a combination between pressure p and self-weight forces. Both effects are studied in a differential volume (dx, dy, dz) within the fluid body in Fig. A. 3 so that the "force term" might be expressed as:

$$\boldsymbol{F} = \int d\boldsymbol{F} \qquad \text{(A. 14)}$$

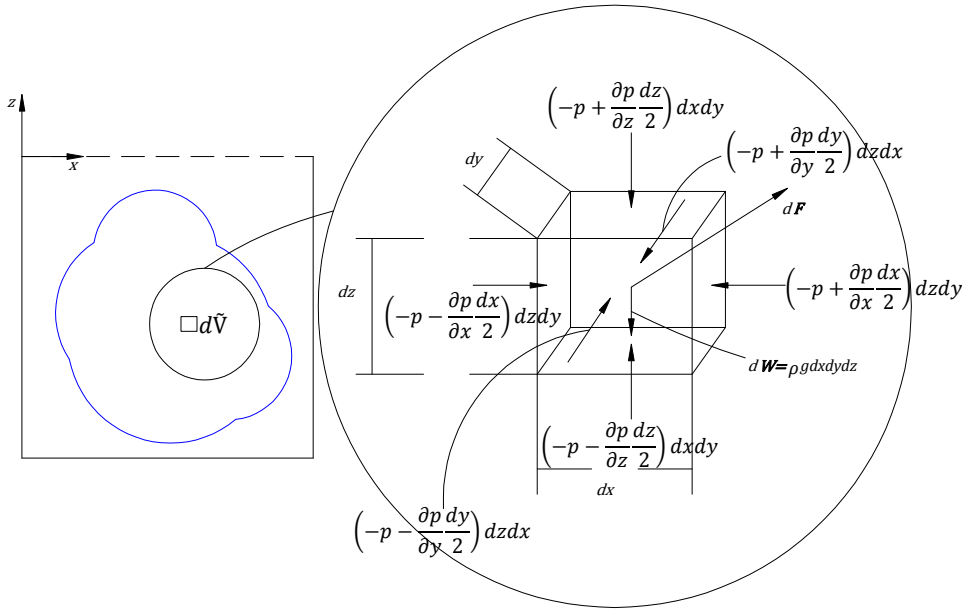

Fig. A. 3. Sketch of surface forces and body forces acting on a differential volume of the fluid body occupying CV at $t0$. The only body force considered is the weight of the differential element and the only surface force considered is the compressive pressure $-p$ as a consequence of assuming inviscid flow.

Therefore, taking into account a compressive pressure ($-p$, in all directions) and the gravitational acceleration, $\boldsymbol{g} = (0,0,-g)$, the "differential force term" in z–direction turns out to be:

$$dF_z = \left(-p-\frac{\partial p}{\partial z}\frac{dz}{2}\right)dxdy - \left(-p+\frac{\partial p}{\partial z}\frac{dz}{2}\right)dxdy - \rho g dzdxdy = \left(-\rho g - \frac{\partial p}{\partial z}\right)d\tilde{\forall} \qquad \text{(A. 15)}$$

The "differential force term" in x and y–directions can be found the same way.

Therefore, since the fluid body is occupying CV at t_0, the "force term" can be rewritten as

$$\boldsymbol{F} = \int_{CV} \left(\rho \boldsymbol{g} - \boldsymbol{\nabla}(p)\right) d\tilde{\mathrm{V}} \tag{A. 16}$$

On the other hand, the area integral regarding $\boldsymbol{P}$ flow through CS can be rewritten into the volume integral of CV by means of the divergence theorem (equation (A. 3)) applied to each of its components. The component in x–direction yields:

$$\int_{CS} u\rho(\boldsymbol{V} \cdot \boldsymbol{n})\, dA = \int_{CV} (\boldsymbol{\nabla} \cdot u\rho \boldsymbol{V}) d\tilde{\mathrm{V}} \tag{A. 17}$$

Therefore, the integrand of the volume integral can be rearranged as:

$$\begin{aligned} \boldsymbol{\nabla} \cdot u\rho\boldsymbol{V} &= \frac{\partial(u\rho u)}{\partial x} + \frac{\partial(u\rho v)}{\partial y} + \frac{\partial(u\rho w)}{\partial z} \\ &= \rho u \frac{\partial(u)}{\partial x} + u\frac{\partial(\rho u)}{\partial x} + \rho v \frac{\partial(u)}{\partial y} + u\frac{\partial(\rho v)}{\partial y} + \rho w \frac{\partial(u)}{\partial z} + u\frac{\partial(\rho w)}{\partial z} \\ &= u\boldsymbol{\nabla} \cdot \rho\boldsymbol{V} + \rho\boldsymbol{V} \cdot \boldsymbol{\nabla}(u) \end{aligned} \tag{A. 18}$$

Same steps are followed for y and z–directions and it will lead to similar expression than equation (A. 18). Hence, the area integral regarding $\boldsymbol{P}$ flow through CS can be rewritten into the volume integral of CV as:

$$\begin{aligned} \int_{CS} \boldsymbol{V}\rho(\boldsymbol{V} \cdot \boldsymbol{n})\, dA &= \int_{CV} \left(\boldsymbol{V}\boldsymbol{\nabla} \cdot \rho\boldsymbol{V} + \rho\boldsymbol{V} \cdot \boldsymbol{\nabla}(\boldsymbol{V})\right) d\tilde{\mathrm{V}} \\ \boldsymbol{\nabla}(\boldsymbol{V}) &= \left(\boldsymbol{\nabla}(u), \boldsymbol{\nabla}(v), \boldsymbol{\nabla}(w)\right) \end{aligned} \tag{A. 19}$$

Where $(\boldsymbol{V})$ is a 2-order tensor containing the gradient vectors of each velocity field component arranged by columns.

Substituting equation (A. 19) and (A. 16) into the linear momentum equation (A. 13) yields:

$$\int_{CV} \left(\frac{\partial(\boldsymbol{V}\rho)}{\partial t} + \boldsymbol{V}\boldsymbol{\nabla} \cdot \rho\boldsymbol{V} + \rho\boldsymbol{V} \cdot \boldsymbol{\nabla}(\boldsymbol{V}) - \left(\rho\boldsymbol{g} - \boldsymbol{\nabla}(p)\right) \right) d\tilde{\mathrm{V}} = \boldsymbol{0} \tag{A. 20}$$

Equation (A. 20) must hold for an arbitrary CV and thus it is just fulfilled when the integrand cancels out.

$$\begin{aligned} \rho\boldsymbol{g} - \boldsymbol{\nabla}(p) &= \frac{\partial(\boldsymbol{V}\rho)}{\partial t} + \boldsymbol{V}\boldsymbol{\nabla} \cdot \rho\boldsymbol{V} + \rho\boldsymbol{V} \cdot \boldsymbol{\nabla}(\boldsymbol{V}) \\ &= \boldsymbol{V}\left(\frac{\partial\rho}{\partial t} + \boldsymbol{\nabla} \cdot \rho\boldsymbol{V}\right) + \rho\left(\frac{\partial\boldsymbol{V}}{\partial t} + \boldsymbol{V} \cdot \boldsymbol{\nabla}(\boldsymbol{V})\right) \end{aligned} \tag{A. 21}$$

The right side of equation (A. 21) can be split into two main parts, a water mass variation with time (mass balance equation) multiplied by $\boldsymbol{V}$ and a velocity variation with time multiplied by ρ. Since linear momentum is defined as the product between mass and velocity, the linear momentum variation with time should contain both mentioned parts. However, if conservation of mass, equation (A. 6), is imposed to equation (A. 21), the water mass variation with time must vanish, so that:

$$\rho \boldsymbol{g} - \boldsymbol{\nabla}(p) = \rho \left(\frac{\partial \boldsymbol{V}}{\partial t} + \boldsymbol{V} \cdot \boldsymbol{\nabla}(\boldsymbol{V}) \right) \quad \text{(A. 22)}$$

Equation (A. 22) is the differential form of the linear momentum equation for an inviscid flow, which is known as Euler's equations of motion.

Nonetheless, an integrated form of equation (A. 22) can be developed.

The weight term ($\rho \boldsymbol{g}$) and the $\boldsymbol{V} \cdot \boldsymbol{\nabla}$ ($\boldsymbol{V}$) term can be expressed as:

$$\rho \boldsymbol{g} = -\rho g \boldsymbol{\nabla}(z) \quad \text{(A. 23)}$$

$$\boldsymbol{V} \cdot \boldsymbol{\nabla}(\boldsymbol{V}) = \frac{1}{2} \boldsymbol{\nabla}(\boldsymbol{V} \cdot \boldsymbol{V}) - \boldsymbol{V} \times \boldsymbol{\omega} \quad \text{(A. 24)}$$

Therefore, assuming irrotational flow, $\boldsymbol{\omega}=\boldsymbol{0}$, equations (A. 9), (A. 23) and (A. 24) are substituted into (A. 22) yielding:

$$-g \boldsymbol{\nabla}(z) - \frac{\boldsymbol{\nabla}(p)}{\rho} = \frac{\partial \left(\boldsymbol{\nabla}(\Phi) \right)}{\partial t} + \boldsymbol{\nabla} \left(\frac{1}{2} \boldsymbol{\nabla}(\Phi) \cdot \boldsymbol{\nabla}(\Phi) \right) \quad \text{(A. 25)}$$

Hereby, the so-called Unsteady Bernoulli's equation for an incompressible fluid and plane irrotational and inviscid flow is obtained integrating equation (A. 25) along an arbitrary direction (i.e. $\int$Equation (A. 25)$\cdot d\boldsymbol{l}$, where $d\boldsymbol{l}=(dx, dy, dz)$), so that:

$$gz + \frac{p}{\rho} + \frac{1}{2} \left(\left(\frac{\partial \Phi}{\partial x} \right)^2 + \left(\frac{\partial \Phi}{\partial z} \right)^2 \right) + \frac{\partial \Phi}{\partial t} = B \quad \text{(A. 26)}$$

Where B is a constant parameter but function of time. B is usually known as the Bernoulli constant.

Since equation (A. 25) was integrated along an arbitrary direction, the Unsteady Bernoulli's equation for an incompressible fluid and plane irrotational and inviscid flow, equation (A. 26), must be fulfilled at every point of the problem domain, like it was also said for Laplace's equation.

A.3. Vorticity field

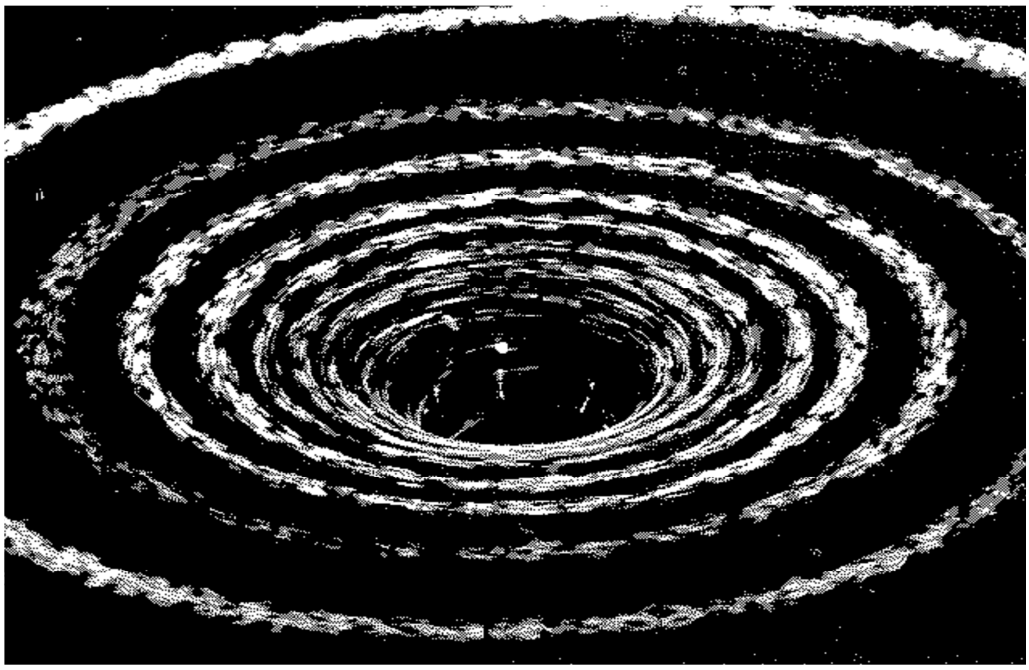

Fig. A. 4. Experiment carried out by the National Committee for Fluid Mechanics Films. The experiment consisted of water passing through a tangential entry of a circular tank, seen from a plan view, and after spiralling round and round in a very tight vortex, the water leaved vertically through a drain located in the centre. The resulting streamline is shown in this figure and it is so tight that it might be thought as being concentric circles.

Fig. A. 4 can illustrate the general pattern behaviour of a vortex. Thus, a vortex could be described as a spiral fluid motion and the resulting streamlines could be regarded as concentric circles.

In order to quantify the observed behaviour, the concept of fluid circulation, Γ, is introduced. Circulation is defined as the line integral of the velocity field $\boldsymbol{V}$ around a closed curve C, Ascher H. Shapiro.[11]

$$\Gamma = \int_C \boldsymbol{V} \cdot d\boldsymbol{r} \tag{A. 27}$$

Where $d\boldsymbol{r}$ is the differential vector tangent to C. Therefore, circulation just accounts for tangential component of the velocity field at C.

In this way, vorticity $\boldsymbol{\omega}$ is defined as circulation around a curve C per unit area when the area enclosed by C tends to 0 (Fig. A. 5(a)).

$$\boldsymbol{\omega} = \omega \boldsymbol{n} = \left(\lim_{dS \to 0} \frac{1}{dS} \int_C \boldsymbol{V} \cdot \boldsymbol{dr} \right) \boldsymbol{n} \tag{A. 28}$$

Where dS is the area enclosed by C and $\boldsymbol{n}$ is its corresponding unitary normal vector.

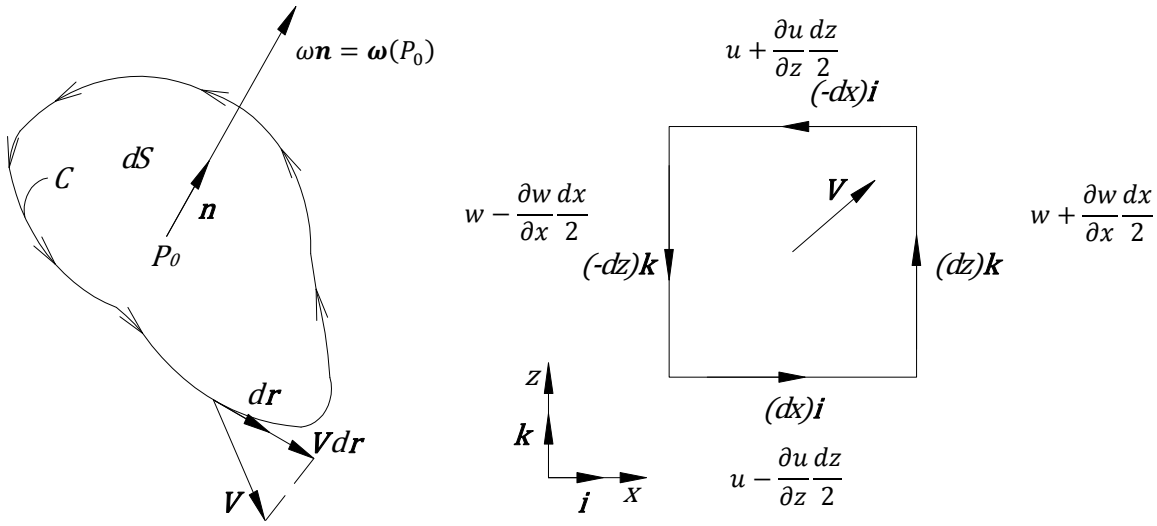

Fig. A. 5. (a) Geometrical interpretation of circulation around C and vorticity at P_0. **(b)** Circulation around a differential closed curve in the x–z–plane caused by $\boldsymbol{V}$. When the area enclosed by such closed curve tends to zero, the resulting circulation will be the y–component of the vorticity field at the point where $\boldsymbol{V}$ is applied.

Therefore, vorticity $\boldsymbol{\omega}$ at a point P_0 given in equation (A. 28)[12] is a vector which can be interpreted as how much the fluid is circulating around a closed curve which encloses a small area ($dS \rightarrow 0$) of geometrical centre P_0 in the direction of $\boldsymbol{n}$ per unit area (Fig. A. 5(a)). Indeed, if P_0 was thought as an infinitesimal small ball and vorticity $\boldsymbol{\omega}$ at P_0 was not null, the ball would be observed to rotate around and axis passing through its geometrical centre due to the fluid circulation around such axis. In this way, it can be imagined a hypothetical case where it was possible to set infinitesimal small balls fixed in the space throughout a flow, so that it would be possible to observe vorticity at every point. If every infinitesimal small ball was not observed to rotate at all, the flow would be irrotational within the observed region.

In order to obtain vorticity in y–direction, a differential square (Fig. A. 5(b)) is considered in the x–z–plane. The circulation throughout the squared closed curve ((dx), (dz), $(-dx)$, $(-dz)$) is:

$$d\Gamma_y = \left(u - \frac{\partial u}{\partial z}\frac{dz}{2}\right)dx + \left(w + \frac{\partial w}{\partial x}\frac{dx}{2}\right)dz + \left(u + \frac{\partial u}{\partial z}\frac{dz}{2}\right)(-dx) + \left(w - \frac{\partial w}{\partial x}\frac{dx}{2}\right)(-dz) = \left(\frac{\partial w}{\partial x} - \frac{du}{\partial z}\right)dxdz \quad \text{(A. 29)}$$

Therefore vorticity in the y–direction is:

$$\omega_y \boldsymbol{j} = \left(\frac{\partial w}{\partial x} - \frac{\partial u}{\partial z}\right)\boldsymbol{j} \quad \text{(A. 30)}$$

Vorticity in x and z–directions can be found in a similar manner.